Proteotoxic stress is a driver of the loser status and of cell competition

Michael E. Baumgartner[#1], Michael P. Dinan [#1,2,§], Paul F. Langton [1], Iwo Kucinski [2,§§], and Eugenia Piddini [1]*

Affiliations

[1] School of Cellular and Molecular Medicine, University of Bristol, Biomedical Sciences Building, University Walk, Bristol BS8 1TD, UK.

[2] The Wellcome Trust/Cancer Research UK Gurdon Institute and Zoology Department, University of Cambridge, Tennis Court Road, Cambridge CB2 1QN, UK.

§ Present address: University of Cambridge, UK

§§ Present address: Wellcome & MRC Cambridge Stem Cell Institute and Department of Haematology, University of Cambridge, UK

[#] Joint first authors

* Correspondence should be addressed to EP: eugenia.piddini@bristol.ac.uk

Keywords: Cell competition, ribosome mutation, ribosomopathy, proteotoxic stress, autophagy, proteasome, *Drosophila*, aneuploidy, FOXO, Rapamycin

Abstract

Cell competition allows “winner” cells to eliminate less fit “loser” cells in tissues. In Minute cell competition, cells heterozygous mutant in ribosome genes, such as *RpS3*$^{+/-}$ cells, are eliminated by wild-type cells. How cells are primed as losers is partially understood and it has been proposed that reduced translation underpins the loser status of ribosome mutant, or *Minute,* cells. Here, using *Drosophila,* we show that reduced translation does not cause cell competition. Instead, we identify proteotoxic stress as the underlying cause of the loser status for Minute competition and competition induced by *mahjong*, an unrelated loser gene. *RpS3*$^{+/-}$ cells exhibit reduced autophagic and proteasomal flux, accumulate protein aggregates, and can be rescued from competition by improving their proteostasis. Conversely, inducing proteotoxic stress is sufficient to turn otherwise wild-type cells into losers. Thus, we propose that tissues may preserve their health through a proteostasis-based mechanism of cell competition and cell selection.

Introduction

Cell competition is a conserved mechanism that allows "winner" cells to eliminate viable but less fit "loser" cells in tissues [1-3]. This process acts as a mechanism of tissue quality control. By removing mis-specified or damaged cells, cell competition preserves tissue and organism health, potentially delaying ageing and disease onset [4-6]. Furthermore, an increasing body of evidence indicates that competitive interactions contribute to tissue colonisation during cancer growth [7].

The first form of competition discovered was Minute cell competition, wherein cells heterozygous mutant in ribosome genes are eliminated by neighbouring wild-type cells [1]. Over 80 genes make up the ribosome, and most display a dominant phenotype when mutated or lost, both in *Drosophila* and humans [8,9]. Based both on phenotypic dominance and on the high number of *Minute* genes, spontaneously occurring Minute cell competition is likely to be a frequent event, relative to other types of cell competition. In addition, as ribosome genes are scattered across chromosomes, Minute cell competition may be frequent in diseases characterized by aneuploidy [10], such as cancer, where deletions of large genomic regions often lead to single copy loss of one or more ribosome genes [11].

Despite its discovery over 40 years ago [1], our understanding of the mechanisms of Minute cell competition remains incomplete [12]. While several signals have been identified that act during cell competition [4,13-19], the upstream signals priming cells as losers are mostly unknown [20]. It is, for instance, unclear how ribosome gene loss leads to the loser status [12]. *Minute* mutants exhibit reduced translation rate [17], and it has long been assumed that this drives the loser status [18,21-25]. However, the actual contribution of translation has not been investigated.

Here, we investigated how ribosome mutations lead to the loser status. We find that translation is not directly linked to the loser status in Minute competition. Instead, we find that ribosome gene mutations lead to defective autophagy and proteasome flux,

accumulation of protein aggregates, and proteotoxic stress. These phenotypes are causative of the loser status. In addition, inducing proteotoxic stress through overexpression of aggregate-prone proteins phenocopies these protein catabolism defects and induces the loser status. Our work identifies proteotoxic stress as the leading cause of the Minute loser status and implicates cell competition in pathologies characterized by proteotoxic stress.

Results

Reduced protein synthesis does not confer the loser status

Minute cell competition is characterized by apoptotic elimination of *Minute* loser cells when they are in proximity of wild-type winner cells [1-3]. Thus, although *Minute* *RpS3*$^{+/-}$ cells display a modest increase in apoptosis compared to wild-type cells when they are in isolation (Figure 1a-b and [26]), apoptosis is substantially elevated during competition in *RpS3*$^{+/-}$ cells that border wild-type cells [12,27,28] (Figure 1c-d). This region-specific induction of apoptosis at clone borders is a hallmark of certain types of cell competition, including Minute competition.

To investigate whether reduced translation triggers cell competition, we expressed a constitutively active form of the translational repressor, 4E-BP (4EBP^{TA}) [29,30], in otherwise wildtype cells. In OPP (O-propargyl-puromycin) and AHA (L-azidohomoalanine) global translation assays, 4EBP^{TA} expression induced a reduction in protein synthesis that was comparable to (Figure 1e-g; OPP) or stronger than (Extended Data Figure 1a-c; AHA) that seen in *RpS3*$^{+/-}$ cells. 4EBP^{TA} expression resulted in little autonomous apoptosis (Figure 1h). Furthermore, the frequency of dying cells was similar at 4EBP^{TA} clone borders and clone centers (Figure 1h-i). These data suggest that reducing rates of global protein synthesis alone, at levels equal to or greater than in *RpS3*$^{+/-}$ cells, is not sufficient to trigger cell competition and indicate that additional properties induced by *RpS3*$^{+/-}$ mutations must also play a role.

We have previously shown that *RpS3*$^{+/-}$ cells and cells mutant in the loser gene and ubiquitin ligase *mahjong* [31] (*mahj*), share what we have termed the 'prospective loser status' – a cellular state which predisposes cells to act as losers when confronted with wildtype winners[20]. This state is characterized by activation of a range of stress response pathways, even in the absence of cell competition [20]. For example, *RpS3*$^{+/-}$ *and mahj*$^{-/-}$ cells display chronic activation of JNK signaling [20,32] and of the Nrf2-mediated oxidative stress response [20]. Furthermore, Nrf2 activation is sufficient to

induce the loser status in competition with wild-type cells [20]. To determine whether a reduction in protein synthesis is sufficient to activate these pathways, we examined the levels of phospho-JNK and the activation of an Nrf2 reporter, GstD1-GFP, in the absence of competition [33]. As Minute cell competition does not occur across compartment boundaries, we are able to use compartment-specific transcriptional drivers to generate wing discs with two distinct but non-competing cell populations, one in the anterior compartment and one in the posterior. Similarly to *RpS3*$^{+/-}$ cells, the levels of phospho-JNK were higher in wing disc cells expressing 4EBP^{TA} than in the wild-type compartment (Figure 1j-k). However, GstD1-GFP levels were only minimally affected in 4EBP^{TA} cells (Figure 1l-n). Thus, a reduction in protein synthesis can produce some aspects of the prospective loser status (JNK activation) but is insufficient to induce oxidative stress response activity or provoke cell competition.

We next asked whether reduced protein synthesis is necessary for *mahj*$^{-/-}$ cells or *RpS3*$^{+/-}$ cells to behave as losers. Knock-down of Mahj did not affect protein translation rate (Extended Data Figure 1d-e), indicating that translation inhibition does not play a role in priming *mahj*$^{-/-}$ cells as losers. Next, we sought to boost rates of translation in *RpS3*$^{+/-}$ cells and assess the resulting effect on the prospective loser status and on Minute competition. GADD34 can stimulate translation via dephosphorylation of the translation initiation factor, eIF2α [34]. Indeed, GADD34 overexpression in *RpS3*$^{+/-}$ cells caused a reduction in phospho-eIF2α (Extended Data Figure 1f-g) and a corresponding rescue of translation, as assessed by OPP incorporation (Figure 1o-p). Surprisingly, GADD34-expressing *RpS3*$^{+/-}$ cells displayed higher levels of the GstD1-GFP oxidative stress reporter (Extended Data Figure 1h-i) and performed worse than *RpS3*$^{+/-}$ cells in competition, with hardly any surviving at the point of dissection (Figure 1q-s). Thus, translation inhibition seems to counter the loser status rather than contribute to it, in *RpS3*$^{+/-}$ cells.

Prospective losers display dependence on autophagy and defective autophagic flux

In order to seek out an alternative cause of the prospective loser status, we turned to a known rescue of Minute competition: inhibition of JNK signaling. In addition to rescuing *RpS3*$^{+/-}$ cells from competition, JNK inhibition partially reverses activation of the transcriptional signature associated with prospective losers [20]. Furthermore, it reduces GstD1-GFP reporter activation in *RpS3*$^{+/-}$ cells (Extended Data Figure 2a). Thus, we compared the transcriptional profiles of *RpS3*$^{+/-}$ wing discs with or without JNK signaling inhibition [20], to identify pathways associated with JNK inhibition and with a rescue of the loser status. This revealed differential expression of genes involved in protein catabolism, the proteasome, autophagy, and the unfolded protein response (Supplementary Table 1). These pathways have all been implicated in Nrf2 regulation [35,36], supporting a potential role in cell competition.

In order to examine the role of autophagy in *RpS3*$^{+/-}$ cells, we obtained wing discs from larvae carrying heterozygous mutations for both *RpS3* and one of several autophagy-related genes: *p62* (*ref(2)P* in *Drosophila*), *atg8* or *atg13* [37]. We found that all three autophagy mutations caused a cell-autonomous increase in apoptotic events in an *RpS3*$^{+/-}$ background, as compared to *RpS3*$^{+/-}$ or autophagy mutations alone (Figure 2a-b, Extended Data Figure 2b-d). Heterozygous mutations in another ribosome loser mutation, *RpL27A*, also caused increased apoptosis in combination with heterozygous mutations in the autophagy gene *p62* (Extended Data Figure 2e-f). Thus, *Minute* cells are acutely reliant on autophagy. However, autophagy inhibition did not impact the competitive status of *RpS3*$^{+/-}$ cells, as knockdown of autophagy genes *atg1* or *atg9* by RNAi did not affect clone coverage or competition-induced cell death in competing *RpS3*$^{+/-}$ cells (except for a mild increase in competitive death in the case of *atg1* RNAi; Extended Data Figure 2g-i). This contrasts with data from Nagata et al., [18], who have instead shown that inhibiting autophagy rescues *Minute* cells from competition. Non-competing *RpS3*$^{+/-}$ cells also appeared to have more atg8-positive foci (Figure 2c) and had more p62-positive foci (Figure 2d-e) than wild-type cells.

Cells with reduced function of the loser gene and ubiquitin ligase *mahj* share with *RpS3*$^{+/-}$ cells a cell-autonomous signature of hundreds of differentially expressed genes

relative to wild-type cells, as well as a cell-autonomous activation of the oxidative stress response [20]. This suggests that mutations in *mahj* and *RpS3* lead to cell competition using a convergent mechanism [20]. Thus, we examined the autophagic state in $mahj^{-/-}$ cells. $mahj^{-/-}$ homozygous clones in a background of $mahj^{+/-}$ and wild type cells also accumulated p62 foci (Figure 2f), whereas $4EBP^{TA}$ had no effect on the number of p62 foci (Figure 2g). Thus, deregulated autophagy is associated with the prospective loser status of two functionally unrelated mutants, and this is not a consequence of reduced protein synthesis.

Accumulation of Atg8- and p62-positive autophagosomes can reflect either decreased or increased autophagic flux [38]. To measure autophagic flux in prospective losers, we designed the reporter "ReFlux" (Ref(2)P autophagy Flux) that measures the rate of p62 degradation [38,39]. p62 is both an autophagy adaptor and an autophagy cargo that is degraded upon autophagosome degradation by the lysosome [38]. Thus, measuring the rate of p62 degradation provides a direct measure of autophagic flux [38]. In ReFlux, p62 is fused to GFP and driven by a *heat-shock* (*hs*) promoter for pulse-chase expression [40] (Figure 2h). As a control, we confirmed that ReFlux reports reduced autophagic flux upon depletion of the autophagy gene *atg1* (Extended Data Figure 3a-c). Then, we expressed ReFlux across wing discs containing $RpS3^{+/-}$ anterior and wild-type posterior compartments. We found that $RpS3^{+/-}$ and wild-type cells show similar GFP-p62 ReFlux signal intensity immediately following pulse expression. However, after a chase period, GFP-p62 ReFlux signal perdures in $RpS3^{+/-}$ cells compared to wild-type cells, indicating reduced autophagic flux (Figure 2i-k). A reduced autophagic flux was also seen in competing $RpS3^{+/-}$ cells, relative to competing wild-type cells (Extended Data Figure 3d-f). Treatment with the autophagy inhibitor chloroquine led to persistence of the GFP-p62 ReFlux signal, confirming that GFP-p62 ReFlux loss is due to autophagic degradation (Extended Data Figure 3g). ReFlux was eventually cleared from the $RpS3^{+/-}$ compartment (Extended Data Figure 3h), indicating that autophagic degradation is delayed but not blocked. Knockdown of Mahj also reduced autophagic flux (Figure 2l-n). Overexpression of $4EBP^{TA}$ also reduced autophagic flux, albeit with a substantially smaller effect size than $RpS3^{+/-}$ mutations (Extended Data Figure 3i-k).

Defective autophagy does not cause the loser status

Defective autophagy has been associated with the loser status in mouse embryonic stem cells [41]. Having observed reduced autophagic flux in both *RpS3*$^{+/-}$ and *mahj*$^{-/-}$ prospective losers, we next investigated whether reduced autophagy is sufficient to induce the loser status in these epithelia. Clones of cells expressing *atg1* RNAi within wild-type imaginal discs did not show cell death enrichment at the clone borders (Figure 3a-b), even though they accumulated p62 foci (Figure 3c), indicative of impaired autophagy. *atg1*-depleted cells also failed to activate the oxidative stress response in a non-competitive context (Figure 3d, right), despite confirmation of autophagy impairment from p62 accumulation (Figure 3d, left). Similarly, inhibiting autophagy in clones by mutating *atg13* caused accumulation of p62 foci (Figure 3e), but did not result in cell competition with wild-type cells, as neither cell death nor clonal disadvantage were observed (Figure 3f-h). Therefore, reduced autophagic flux is observed in *RpS3*$^{+/-}$ cells both in the absence of and during competition but is not sufficient to cause cell competition.

As reduced protein synthesis and autophagy flux are observed in *RpS3*$^{+/-}$ losers but neither is sufficient to confer the loser status, we asked whether they might do so in concert. However, co-expressing *atg9* RNAi and 4EBP^{TA} in clones of cells in a wild-type wing disc did not result in border cell death, indicating that reduced protein synthesis and defective autophagy together are not sufficient to induce the competitive elimination of losers (Figure 3i-k).

Prospective losers have defective proteasome flux

Proteasome genes were also differentially expressed in *RpS3*$^{+/-}$ cells upon JNK signaling inhibition (Supplementary Table 1), prompting us to investigate the role of the proteasome in *Minute* cells. Heterozygosity of a proteasomal core subunit gene caused increased apoptosis in *RpS3*$^{+/-}$ cells and in *RpL27A*$^{+/-}$ cells (Extended Data Figure 4a-

d). Similarly, feeding flies the proteasome inhibitor bortezomib [42] increased the number of dying cells in *RpS3*$^{+/-}$ but not wild-type wing discs (Figure 4a-c). Thus, ribosome mutant cells are cell-autonomously reliant on proteasome function in addition to autophagy.

To determine whether proteasome function is dysregulated in *RpS3*$^{+/-}$ cells, we examined proteasome activity with CL1-GFP, a fusion of GFP with the proteasome degradation signal CL1, which targets GFP for efficient proteasomal degradation[43]. To enhance reporter sensitivity, we designed the reporter ProteoFlux, a *hs*-driven CL1-GFP, to enable pulse-chase measurements of proteasome flux (Figure 4d). We confirmed that ProteoFlux CL1-GFP detects reduced proteasome flux when we interfere with proteasome function by knockdown of the proteasome subunit Rpt6 (Figure 4e-f). We then expressed ProteoFLUX CL1-GFP in wing discs harboring *RpS3*$^{+/-}$ anterior and wild-type posterior compartments, so that we could compare directly their proteasome flux in the absence of cell competition. *RpS3*$^{+/-}$ and wild-type cells showed similar ProteoFLUX CL1-GFP signal intensity immediately after pulse expression. After a chase period, however, we observed higher GFP intensity in *RpS3*$^{+/-}$ than in wild-type cells, indicating slower proteasome flux in *RpS3*$^{+/-}$ cells (Figure 4g-i). ProteoFlux CL1-GFP degradation was also delayed in cells depleted for Mahj (Extended Data Figure 4e-g), but not in 4EBP^{TA}-expressing cells (Extended Data Figure 4h-j). Therefore, like reduced autophagic flux, reduced proteasomal flux is a common feature of genetically distinct prospective losers.

RpS3$^{+/-}$ mutations induce protein aggregates and stoichiometric imbalance in ribosome proteins

Ribosomal proteins are degraded by the proteasome [44] and by autophagy [45,46]. Indeed, electron microscopy analysis showed phago-lysosomal structures containing ribosomes both in wild-type and in *RpS3*$^{+/-}$ wing disc cells (Extended Data Figure 4k). We reasoned that *RpS3*$^{+/-}$ mutations could lead to a stoichiometric imbalance in ribosome proteins, which could in turn cause proteotoxic stress and overload the

proteasome and autophagy machineries [47,48]. To test this, we measured relative levels of ribosome proteins, by Tandem Mass Tag (TMT) Spectrometry of *RpS3*$^{+/-}$ and wild-type wing discs. TMT successfully identified 78 ribosome proteins of the 93 reported on Flybase (of the missing 15, 8 are not expected to be expressed in wing discs). This showed that the *RpS3*$^{+/-}$ mutation causes a reduction in RpS3 protein of 0.291 log-fold relative to wild-type levels. Interestingly, a reduction was observed for all small ribosome subunit proteins detected (Figure 4j), indicating coordinated regulation, but this was not seen for components of the large subunit, whose levels were, with few exceptions, equal to or higher than in wild-type cells (Figure 4j). Thus, at steady state, *RpS3*$^{+/-}$ cells have a stoichiometric excess of ribosome proteins from the large subunit relative to small subunit ribosome proteins. This could contribute to proteasome and autophagy overload.

When they are not efficiently cleared by degradation, ribosome proteins can form protein aggregates [44,47,48]. To test this, we used Proteostat, a dye which fluoresces upon intercalation with protein aggregate-associated quaternary structures. Indeed, Proteostat staining detected accumulation of protein aggregates in *RpS3*$^{+/-}$ cells relative to wild-type cells, in the absence of cell competition (Figure 4k). Protein aggregates are often ubiquitin-positive [49,50], and immunostaining with the FK2 antibody, which detects mono- and poly-ubiquitin conjugates, revealed that *RpS3*$^{+/-}$ cells, but not wild-type cells, accumulate large, ubiquitin-positive foci in the cytoplasm (Figure 4l). Many of these foci were also positive for the autophagy adapter/cargo p62 (Figure 4l), which is often recruited to cytosolic protein aggregates [50]. Furthermore, phospho-eIF2α, a marker of proteotoxic stress and of the integrated stress response [34], was upregulated in *RpS3*$^{+/-}$ cells, both in homotypic conditions (Extended Data Figure 4l-m) and during cell competition (Extended Data Figure 4n-o). Collectively, *RpS3*$^{+/-}$ cells show reduced autophagy flux, reduced proteasome flux, accumulation of ubiquitinated protein aggregates, and markers of proteotoxic stress.

Improving proteostasis in *RpS3*$^{+/-}$ cells rescues their loser status

Proteotoxic stress can induce Nrf2 activation [51], and this in turn is linked to the loser status [20], suggesting a link between proteotoxic stress and the prospective loser status. Consistent with this, inhibiting the proteasome with bortezomib was sufficient to elevate GstD1-GFP signal in non-competing wild-type and *RpS3*$^{+/-}$ wing disc cells (Extended Data Figure 5a-c). We therefore asked whether alleviating proteotoxic stress would rescue loser cells from competition. Rapamycin inhibits TOR signaling and promotes proteostasis via multiple mechanisms, including inhibiting translation and activating autophagy and proteasome functions [52,53]. We found that rapamycin feeding reduced the frequency of competition-induced apoptosis in *RpS3*$^{+/-}$ cells bordering wild-type cells (Figure 5a-c). Rapamycin feeding also reduced the cell-autonomous activation of the oxidative stress reporter GstD1-GFP in *RpS3*$^{+/-}$ cells (Figure 5d-e). As rapamycin was fed systemically, the observed rescue of competition-induced cell death could in part arise from the effects of rapamycin on wild-type cells. We therefore sought to improve proteostasis specifically in *RpS3*$^{+/-}$ cells. To this end, we overexpressed, in *RpS3*$^{+/-}$ cells, the transcription factor FOXO, which is inhibited by TOR signaling [54,55] and promotes both autophagy and proteasome functions [55]. FOXO overexpression reduced the number of p62-positive aggregates (Figure 5f), increased protein synthesis (Figure 5g-h) and reduced mildly the levels of phospho-eIF2α (Figure 5i-j) in *RpS3*$^{+/-}$ cells, indicating overall improved proteostasis. Strikingly, FOXO overexpression in *RpS3*$^{+/-}$ cells abolished competition-induced cell death, as very few apoptotic bodies could be detected in competition with wild-type cells (Figure 5k-m). These data indicate that reducing proteotoxic stress inhibits the competitive elimination of *RpS3*$^{+/-}$ cells.

Proteotoxic stress in sufficient to cause the loser status

We considered that protein aggregation and proteotoxic stress could be sufficient to cause the loser status in competitive contexts. To test this hypothesis, we ectopically expressed the human aggregate-prone polyQ protein ataxin-3 (SCA3/MJDQ78), which is responsible for the human neurodegenerative disorder Machado Joseph Disease [56]

329 and has been used in *Drosophila* to model this neurodegenerative condition [57]. MJDQ78
330 expression was sufficient to recapitulate many features shared by *RpS3*$^{+/-}$ and *mahj*$^{-/-}$
331 prospective losers, namely up-regulation of GstD1-GFP (Figure 6a-b), reduced
332 autophagic flux (Figure 6c), and accumulation of p62-positive structures (Figure 6d-e).
333 MJDQ78 however, did not perceptibly impact on rates of translation, as measured by
334 OPP incorporation (Figure 6f-g). Importantly, clones overexpressing MJDQ78 in wild-
335 type wing disc showed a local induction of apoptosis, specifically at their borders with
336 wild-type cells (Figure 6h-i), and grew poorly relatively to wild-type clones (Figure 6j-l),
337 indicating that these cells are eliminated by cell competition. This was specifically
338 induced by proteotoxic stress, as clones expressing the wild-type version of Ataxin-3
339 (MJDQ27) [57] did not show induction of border death (Extended Data Figure 5d-f). Thus,
340 proteotoxic stress is sufficient to turn otherwise wild-type cells into losers (Figure 6m).
341

Discussion

Our work shows that single copy loss of ribosome genes leads to major defects in cellular proteostasis, as also shown in the accompanying paper from Recanses-Alvarez et al., [58]. Heterozygosity of ribosome genes in humans leads to genetic disorders collectively known as ribosomopathies, characterized by severe malformations and pathologies [9]. The mechanisms through which ribosomal mutations lead to these defects are only partially understood [9]. Our work suggests that proteotoxic stress may be an underlying cause for some such defects and that they might be improved by drugs that promote proteostasis, such as the FDA-approved compound rapamycin [53] that we have used in this study.

Our work shows that proteotoxic stress is sufficient to confer the loser status. This finding broadens the scope of cell competition and suggests it may be an active mechanism in physiological and pathological contexts characterized by proteotoxic stress. This may help explain the competitive elimination of neurons in *Drosophila* models of neurodegenerative diseases [59]. It may be especially relevant to cancer, where proteotoxic stress is often observed [60]. Our findings suggest that cancer cells might represent concealed losers that have escaped proteotoxic stress-induced cell competition through masking mutations. Understanding how *Minute* mutations and proteotoxic stress lead to cell competition may help unmask the loser status in cancer cells in ways that could be exploited therapeutically [7].

Healthy proteostasis is a driver of organism fitness [61] and contributes to organism longevity [62], whereas impaired proteostasis is associated with aging and with age-related pathologies [62, 63]. We propose that tissues preserve their health and youth through a proteostasis-based mechanism of cell elimination. By measuring cell fitness on the basis of proteostasis and converting it into the loser status through the activation of the oxidative stress response, proteostasis-based cell competition could act as a general mechanism of cell selection in adult homeostasis. How proteotoxic stress induces the loser status remains to be established.

Acknowledgments

We thank the Piddini group for input on the project and manuscript, Rafael Carazo Salas for feedback and discussions on the data and Life Science Editors for editorial assistance. We thank the Wolfson Bioimaging Facility for access to microscopes and for assistance in performing electron microscopy. We also thank the University of Bristol Proteomics Facility for performing the TMT proteomic experiments and for proteomics bioinformatics support. We are grateful to Tor Erik Rusten for the generous gift of the p62 antibody. This work was supported by Wellcome Trust PhD studentships to MPD and to IK, a Cancer Research UK Programme Grant to E.P (A12460), a Cancer Research UK Programme Foundation Award to E.P. (Grant C38607/A26831) and a Royal Society University Research fellowship to E.P. (UF0905080). E.P. is a Wellcome Trust Senior Research Fellow (205010/Z/, 16/Z).

Author contributions: E.P. led the project. All authors conceived the experiments. M.P.D, M.B, I.K. and P.F.L performed and analysed the experiments. M.P.D, M.B, P.F.L and E.P. wrote the manuscript.

Financial and non-financial competing interests: The authors declare no competing interests.

Materials & correspondence: The Lead Contact, Eugenia Piddini (ep16996@bristol.ac.uk), will fulfil requests for resources and reagents.

References

1. Morata, G. & Ripoll, P. Minutes: mutants of drosophila autonomously affecting cell division rate. *Developmental Biology* **42,** 211–221 (1975).
2. Baker, N. E. Mechanisms of cell competition emerging from Drosophila studies. *Curr. Opin. Cell Biol.* **48,** 40–46 (2017).
3. Maruyama, T. & Fujita, Y. Cell competition in mammals - novel homeostatic machinery for embryonic development and cancer prevention. *Curr. Opin. Cell Biol.* **48,** 106–112 (2017).
4. Merino, M. M. *et al.* Elimination of unfit cells maintains tissue health and prolongs lifespan. *Cell* **160,** 461–476 (2015).
5. Brown, S. *et al.* Correction of aberrant growth preserves tissue homeostasis. *Nature* **548,** 334–337 (2017).
6. Liu, N. *et al.* Stem cell competition orchestrates skin homeostasis and ageing. *Nature* **568,** 344–350 (2019).
7. Vishwakarma, M. & Piddini, E. Outcompeting cancer. *Nature Reviews Cancer* **20,** 187–198 (2020).
8. Marygold, S. J. *et al.* The ribosomal protein genes and Minute loci of Drosophila melanogaster. *Genome Biol* **8,** R216 (2007).
9. Mills, E. W. & Green, R. Ribosomopathies: There's strength in numbers. *Science* **358,** eaan2755 (2017).
10. Baker, N. E. Cell competition. *Curr. Biol.* **21,** R11–5 (2011).
11. Ajore, R. *et al.* Deletion of ribosomal protein genes is a common vulnerability in human cancer, especially in concert with TP53 mutations. *EMBO Mol Med* **9,** 498–507 (2017).
12. Baker, N. E. Emerging mechanisms of cell competition. *Nat. Rev. Genet.* **29,** 1–15 (2020).
13. Rhiner, C. *et al.* Flower Forms an Extracellular Code that Reveals the Fitness of a Cell to its Neighbors in Drosophila. *Dev. Cell* **18,** 985–998 (2010).
14. Meyer, S. N. *et al.* An ancient defense system eliminates unfit cells from developing tissues during cell competition. *Science* **346,** 1258236 (2014).
15. Baillon, L., Germani, F., Rockel, C., Hilchenbach, J. & Basler, K. Xrp1 is a transcription factor required for cell competition-driven elimination of loser cells. *Sci Rep* **8,** 17712–10 (2018).
16. Kale, A., Li, W., Lee, C.-H. & Baker, N. E. Apoptotic mechanisms during competition of ribosomal protein mutant cells: roles of the initiator caspases Dronc and Dream/Strica. *Cell Death Differ* **22,** 1300–1312 (2015).
17. Lee, C.-H. *et al.* A Regulatory Response to Ribosomal Protein Mutations Controls Translation, Growth, and Cell Competition. *Dev. Cell* **46,** 456–469.e4 (2018).
18. Nagata, R., Nakamura, M., Sanaki, Y. & Igaki, T. Cell Competition Is Driven by Autophagy. *Dev. Cell* **51,** 99–112.e4 (2019).
19. Blanco, J., Cooper, J. C. & Baker, N. E. Roles of C/EBP class bZip proteins in the growth and cell competition of Rp ('Minute') mutants in Drosophila. *Elife* **9,** 5184 (2020).

20. Kucinski, I., Dinan, M., Kolahgar, G. & Piddini, E. Chronic activation of JNK JAK/STAT and oxidative stress signalling causes the loser cell status. *Nature Communications* **8,** 136 (2017).
21. Kale, A. *et al.* Ribosomal Protein S12e Has a Distinct Function in Cell Competition. *Dev. Cell* **44,** 42–55.e4 (2018).
22. Lee, C.-H. *et al.* A Regulatory Response to Ribosomal Protein Mutations Controls Translation, Growth, and Cell Competition. *Dev. Cell* **46,** 807 (2018).
23. Milán, M. Survival of the fittest. Cell competition in the Drosophila wing. *EMBO reports* **3,** 724–725 (2002).
24. Moreno, E. & Basler, K. dMyc transforms cells into super-competitors. *Cell* **117,** 117–129 (2004).
25. Amoyel, M. & Bach, E. A. Cell competition: how to eliminate your neighbours. *Development* **141,** 988–1000 (2014).
26. Coelho, C. M. A. Growth and cell survival are unevenly impaired in pixie mutant wing discs. *Development* **132,** 5411–5424 (2005).
27. Moreno, E., Basler, K. & Morata, G. Cells compete for decapentaplegic survival factor to prevent apoptosis in Drosophila wing development. *Nature* **416,** 755–759 (2002).
28. Li, W. & Baker, N. E. Engulfment is required for cell competition. *Cell* **129,** 1215–1225 (2007).
29. Imai, Y. *et al.* Phosphorylation of 4E-BP by LRRK2 affects the maintenance of dopaminergic neurons in Drosophila. *The EMBO Journal* **27,** 2432–2443 (2008).
30. Mader, S., Lee, H., Pause, A. & Sonenberg, N. The translation initiation factor eIF-4E binds to a common motif shared by the translation factor eIF-4 gamma and the translational repressors 4E-binding proteins. *Molecular and Cellular Biology* **15,** 4990–4997 (1995).
31. Tamori, Y. *et al.* Involvement of Lgl and Mahjong/VprBP in Cell Competition. *Plos Biol* **8,** e1000422 (2010).
32. Tamori, Y. & Deng, W.-M. Cell competition and its implications for development and cancer. *Journal of Genetics and Genomics* **38,** 483–495 (2011).
33. Sykiotis, G. P. & Bohmann, D. Keap1/Nrf2 signaling regulates oxidative stress tolerance and lifespan in Drosophila. *Dev. Cell* **14,** 76–85 (2008).
34. Pakos-Zebrucka, K. *et al.* The integrated stress response. *EMBO reports* **17,** 1374–1395 (2016).
35. Jain, A. *et al.* p62/Sequestosome-1, Autophagy-related Gene 8, and Autophagy in Drosophila Are Regulated by Nuclear Factor Erythroid 2-related Factor 2 (NRF2), Independent of Transcription Factor TFEB. *Journal of Biological Chemistry* **290,** 14945–14962 (2015).
36. Silva-Islas, C. A. & Maldonado, P. D. Canonical and non-canonical mechanisms of Nrf2 activation. *Pharmacol. Res.* **134,** 92–99 (2018).
37. Lamb, C. A., Yoshimori, T. & Tooze, S. A. The autophagosome: origins unknown, biogenesis complex. *Nat Rev Mol Cell Biol* **14,** 759–774 (2013).
38. Mauvezin, C., Ayala, C., Braden, C. R., Kim, J. & Neufeld, T. P. Assays to monitor autophagy in Drosophila. *Methods* **68,** 134–139 (2014).
39. Chang, Y.-Y. & Neufeld, T. P. An Atg1/Atg13 complex with multiple roles in TOR-mediated autophagy regulation. *Mol. Biol. Cell* **20,** 2004–2014 (2009).

40. Piddini, E., Marshall, F., Dubois, L., Hirst, E. & Vincent, J.-P. Arrow (LRP6) and Frizzled2 cooperate to degrade Wingless in Drosophila imaginal discs. *Development* **132,** 5479–5489 (2005).
41. Sancho, M. *et al.* Competitive interactions eliminate unfit embryonic stem cells at the onset of differentiation. *Dev. Cell* **26,** 19–30 (2013).
42. Paramore, A. & Frantz, S. Bortezomib. *Nat Rev Drug Discov* **2,** 611–612 (2003).
43. Pandey, U. B. *et al.* HDAC6 rescues neurodegeneration and provides an essential link between autophagy and the UPS. *Nature* **447,** 859–863 (2007).
44. Sung, M.-K., Reitsma, J. M., Sweredoski, M. J., Hess, S. & Deshaies, R. J. Ribosomal proteins produced in excess are degraded by the ubiquitin-proteasome system. *Mol. Biol. Cell* **27,** 2642–2652 (2016).
45. Kraft, C., Deplazes, A., Sohrmann, M. & Peter, M. Mature ribosomes are selectively degraded upon starvation by an autophagy pathway requiring the Ubp3p/Bre5p ubiquitin protease. *Nature Publishing Group* **10,** 602–610 (2008).
46. Wyant, G. A. *et al.* NUFIP1 is a ribosome receptor for starvation-induced ribophagy. *Science* **360,** 751–758 (2018).
47. Tye, B. W. *et al.* Proteotoxicity from aberrant ribosome biogenesis compromises cell fitness. *Elife* **8,** 3429 (2019).
48. Albert, B. *et al.* A ribosome assembly stress response regulates transcription to maintain proteome homeostasis. *Elife* **8,** 720 (2019).
49. Rubinsztein, D. C. The roles of intracellular protein-degradation pathways in neurodegeneration. *Nature* **443,** 780–786 (2006).
50. Nezis, I. P. *et al.* Ref(2)P, the Drosophila melanogaster homologue of mammalian p62, is required for the formation of protein aggregates in adult brain. *J. Cell Biol.* **180,** 1065–1071 (2008).
51. Cullinan, S. B. & Diehl, J. A. PERK-dependent activation of Nrf2 contributes to redox homeostasis and cell survival following endoplasmic reticulum stress. *J. Biol. Chem.* **279,** 20108–20117 (2004).
52. Bjedov, I. *et al.* Mechanisms of Life Span Extension by Rapamycin in the Fruit Fly Drosophila melanogaster. *Cell Metabolism* **11,** 35–46 (2010).
53. Li, J., Kim, S. G. & Blenis, J. Rapamycin: one drug, many effects. *Cell Metabolism* **19,** 373–379 (2014).
54. Laplante, M. & Sabatini, D. M. mTOR Signaling. *Cold Spring Harbor Perspectives in Biology* **4,** (2012).
55. Webb, A. E. & Brunet, A. FOXO transcription factors: key regulators of cellular quality control. *Trends in Biochemical Sciences* (2014). doi:10.1016/j.tibs.2014.02.003
56. Klockgether, T., Mariotti, C. & Paulson, H. L. Spinocerebellar ataxia. *Nat Rev Dis Primers* **5,** 24–21 (2019).
57. Bonini, N. M. A genetic model for human polyglutamine-repeat disease in Drosophila melanogaster. *Philos. Trans. R. Soc. Lond., B, Biol. Sci.* **354,** 1057–1060 (1999).
58. Recasens-Alvarez, C., Alexandre, C., Kirkpatrick, J., Nojima, H., Huels, D. J., Snijders, A. P., & Vincent, J.-P. Ribosomopathy-associated mutations cause proteotoxic stress that is alleviated by TOR inhibition. *Nature Cell Biology* (2020).

59. Coelho, D. S. *et al.* Culling Less Fit Neurons Protects against Amyloid-β-Induced Brain Damage and Cognitive and Motor Decline. *CellReports* **25,** 3661–3673.e3 (2018).
60. Guang, M. H. Z. *et al.* Targeting Proteotoxic Stress in Cancer: A Review of the Role that Protein Quality Control Pathways Play in Oncogenesis. *Cancers* **11,** 66 (2019).
61. Jarosz, D. F., Taipale, M. & Lindquist, S. Protein homeostasis and the phenotypic manifestation of genetic diversity: principles and mechanisms. *Annu. Rev. Genet.* **44,** 189–216 (2010).
62. Kaushik, S. & Cuervo, A. M. Proteostasis and aging. *Nat Med* **21,** 1406–1415 (2015).
63. Taylor, R. C. & Dillin, A. Aging as an Event of Proteostasis Collapse. *Cold Spring Harbor Perspectives in Biology* **3,** a004440–a004440 (2011).

Figure Legends

Figure 1. Reduced protein synthesis does not confer the loser status.

(**a**-**b**) Apoptosis detection by cleaved caspase-3 staining (red) in wild type or *RpS3*$^{+/-}$ non-competing (homotypic) wing discs (**a**) and corresponding quantification (n=7 and 10, respectively, two-sided Mann-Whitney U Test) (**b**). (**c**-**d**) Apoptosis detection by dcp-1 staining (red) in competing wing discs containing *RpS3*$^{+/-}$ cells (GFP-positive) and unlabeled wild type cells (GFP-negative) (**c**) and corresponding quantification (n=8, two-sided Wilcoxon signed-rank test) (**d**). (**e**-**g**) Translation rate measurement by OPP in wing discs containing wild-type cells and *RpS3*$^{+/-}$ clones (GFP-positive) (**e**) or 4E-BP^{TA}-expressing clones (GFP-positive) (**f**). Corresponding quantifications are in (**g**) (n=10 and 10 respectively, two-sided two sample Kolmgorov-Smirnov test). (**h**-**i**) Apoptosis detection by cleaved caspase-3 staining (red) in wing discs with mosaic expression of 4E-BP^{TA} (GFP-positive) (**h**), and corresponding cell death quantifications (n=9, two-sided Wilcoxon signed-rank test) (**i**). (**j**) Wing disc harboring an *RpS3*$^{+/-}$ Anterior (A) and a wild-type Posterior (P) compartments stained for anti-active phospho-JNK (p-JNK, red). (**k**) Wing disc expressing 4E-BP^{TA} in P compartment stained for p-JNK (red). (**l-n**) *GstD1*-GFP signal (green) in wing discs harboring *RpS3*$^{+/-}$ A cells (dsRed-positive) and wild-type P cells (dsRed-negative) (**l**) and in wing discs harboring 4E-BP^{TA}-expressing P and wild-type A cells (**m**), and corresponding quantification (n=12 and 10 respectively, two-sided two sample Kolmgorov-Smirnov test) (**n**). (**o-p**) An *RpS3*$^{+/-}$ wing disc over-

expressing GADD34 in P cells and labelled with OPP (**o**), and corresponding quantification (n=5, two-sided paired t-test) (**p**). (**q-s**) Wing discs harboring wild-type cells and *RpS3*$^{+/-}$ clones (GFP-positive) (**q**) or *RpS3*$^{+/-}$ clones expressing GADD34 (GFP-positive) (**r**), and corresponding quantification (n=17 and 10 respectively, two-sided Mann-Whitney U test) (**s**). In this figure, for all micrographs, scale bars correspond to 50µm. All n numbers refer to the number of individual wing discs. In this figure and throughout: dashed lines indicate wing pouch or clonal and compartment boundaries; clone border defines cells within 2-cell diameters of the clone perimeter; Posterior is right and dorsal is up; figure panel genotypes are provided for all figures in Supplementary Table 3; each point in graphs represents one wing disc, unless otherwise indicated. For all quantifications, the horizontal line represents the mean and whiskers indicate 95% confidence intervals.

Figure 2. Prospective losers display defective autophagic flux.

(**a**-**b**) Apoptotic cell death, as detected by anti-cleaved Caspase-3 reactivity (green), in wing discs of a *p62*$^{+/-}$ heterozygote (**a**, left), *RpS3*$^{+/-}$ heterozygote (**a**, middle), or *p62*$^{+/-}$, *RpS3*$^{+/-}$ transheterozygote (**a**, right) and corresponding quantification (n=10, 7, and 11 respectively, two-sided Mann-Whitney U test without p-adjustment for multiple comparisons) (**b**). (**c**) Staining of autophagosomes and autolysosomes, as detected by atg8-GFP-mCherry expression (red) in the P-compartment of wild type (**c,** left), or *Rps3*$^{+/-}$ (**c,** right) wing discs. (**d**-**e**) Immunostaining for p62 in wing discs harboring *RpS3*$^{+/-}$ A cells and wild type P cells (**d**) and corresponding fluorescence intensity quantification (n=9, two-sided paired t-test) (**e**). (**f**) Immunostaining of p62 in a wing disc with *mahj*$^{-/-}$ clones (GFP-negative) induced in a *mahj*$^{+/-}$ heterozygous background (1XGFP). Wild-type twin spots are 2XGFP. (**g**) Immunostaining for p62 in wing discs harboring wild-type A cells and 4E-BP^{TA}-expressing P cells (labelled by the absence of Ci, magenta). (**h**) Schematic representation of ReFLUX: the autophagy cargo p62 is fused to GFP and driven by a *hs* promoter for pulse-chase expression. (**i-k**) GFP-p62 ReFlux signal (green) in wing discs harboring *RpS3*$^{+/-}$ A cells (dsRed-positive) and wild-type P cells (dsRed-negative) immediately after heat shock (**i**), or three hours later (**j**)

and corresponding signal quantifications (n= 7 and 8 respectively, two-sided student's t-test) (**k**). (**l-n**) GFP-p62 ReFlux signal (green) in wing discs expressing *mahj*-RNAi in the P compartment (RFP-positive), immediately after heat shock (**l**) or three hours later (**m**) and corresponding signal quantifications (n=8 and 7 respectively, two-sided student's t-test) (**n**). For all micrographs, scale bars correspond to 50µm. For all quantification, the horizontal line represents the mean and whiskers indicate 95% confidence intervals. All n numbers refer to the number of individual wing discs.

Figure 3. Autophagy impairment does not confer the loser status. (**a**-**b**) Apoptosis detection by cleaved caspase-3 staining (red) in wing discs with mosaic expression of *atg1*-RNAi (GFP-positive cells) (**a**) and corresponding quantifications (n=9, two-sided Wilcoxon signed-rank test) (**b**). Cell death is classed as border death or center death, as described in Figure 1. (**c**) p62 staining in wing discs of the same genotype as in (**a**). (**d**) p62 staining (left) and *GstD1*-GFP signal (right) in wing discs harboring *atg1*-RNAi expressing P cells and wild-type A cells. (**e**-**h**) p62 staining (**e**) and apoptosis detection by cleaved caspase-3 staining (red) (**f**) in wing discs with *atg13*$^{-/-}$ clones (GFP-negative) induced in an *atg13*$^{+/-}$ heterozygous background (1XGFP), and corresponding cell death (**g**, n=12, two-sided Wilcoxon signed-rank test) and clone size (**h**, n=95 and 105, respectively, two-sided Mann-Whitney U test) quantifications for *atg13*$^{-/-}$ clones and wild-type *atg13*$^{+/+}$ twin spots (2XGFP). Each dot or square on the graph in (**h**) represents one clone, and the horizontal line represents the median and whiskers indicate the 95% confidence interval. (**i-k**) Wing discs harboring GFP-positive clones expressing *atg9-RNAi* (**j**) or expressing *atg9-RNAi* and 4E-BP^{TA} (**k**) and stained for cleaved-dcp1 (red) and corresponding cell death quantification in clone centers (Cent.) versus borders (Bord.) (n=11 and 14 respectively, two-sided Wilcoxon signed-rank test) (**i**). For all micrographs, scale bars correspond to 50µm. For all quantifications provided other than (**h**), the horizontal line represents the mean and whiskers indicate 95% confidence intervals. All n numbers refer to the number of individual wing discs, except in (**h**) wherein n numbers refer to the number of individual twin-spot clones.

Figure 4. Prospective losers display proteotoxic stress. (**a**-**b**) Apoptosis detection by cleaved caspase-3 staining (red) in wild type (**a**) or *RpS3*$^{+/-}$ (**b**) wing discs fed DMSO or 10 μM bortezomib, as indicated. (**c**) Quantification of dying cell numbers within the pouch region of wing discs from the conditions indicated in (**a**-**b**) (n=8, 8, 7, and 5, respectively, two-sided Mann-Whitney U test without p-adjustment for multiple comparisons). (**d**) Schematic representation of ProteoFLUX: a fusion of GFP with the proteasome degradation signal CL1, driven by a *hs* promoter for pulse-chase expression. (**e**-**f**) ProteoFLUX CL1-GFP signal (green) in wing discs expressing RNAi against the proteasomal subunit *Rpt6* specifically in P cells, immediately after heat shock or two hours later, as indicated (**e**), and corresponding signal quantifications (n=3 and 11 respectively, two-sided Mann-Whitney U test) (**f**). (**g**-**i**) ProteoFLUX CL1-GFP signal (green) in wing discs harboring *RpS3*$^{+/-}$ A cells (dsRed-positive) and wild-type P cells (dsRed-negative), immediately after heat shock (**g**), or two hours later (**h**), and corresponding signal quantifications (n=7 and 7 respectively, two-sided student's t-test) (**i**). (**j**) Abundance of Ribosomal subunit proteins in *RpS3*$^{+/-}$ wing discs relative to wild-type wing discs by TMT Mass Spectrometry. Bars indicate average log fold change values across two independent biological replicates. (**k**) Proteostat protein aggregate staining (green) in wing discs harboring *RpS3*$^{+/-}$ A cells and wild-type P cells. (**l**) FK2 anti-conjugated ubiquitin (green) and anti-p62 (red) staining in a wing disc harboring an *RpS3*$^{+/-}$ A compartment and a wild-type P compartment, as indicated. Yellow boxes mark inset locations. For all micrographs, scale bars correspond to 50μm. For all quantifications provided, the horizontal line represents the mean and whiskers indicate 95% confidence intervals. All n numbers refer to the number of individual wing discs.

Figure 5. Alleviating proteotoxic stress rescues the loser status. (**a**-**b**) Apoptosis detection by cleaved caspase-3 staining (red) in competing wing discs containing *RpS3*$^{+/-}$ cells (GFP-positive) and unlabeled wild type cells (GFP-negative) from larvae fed ethanol carrier (**a**) or 4 μM rapamycin (**b**). (**c**) Quantification of cell death at *RpS3*$^{+/-}$ clone boundaries for the experiments in (**a**-**b**) (n=13 and 12 respectively, two-sided two sample Kolmgorov-Smirnov test). (**d-e**) *GstD1*-GFP signal (green) in *RpS3*$^{+/-}$ wing discs fed EtOH control or 4μM Rapamycin, as indicated (**d**), and corresponding quantification

(n=10 and 12 respectively, two-sided student's t-test) (**e**). (**f**) p62 staining in *RpS3*$^{+/-}$ wing discs expressing FOXO in P cells (labelled by the absence of Ci, magenta). (**g-h**) An *RpS3*$^{+/-}$ wing disc harboring FOXO expressing clones (GFP-positive) and labelled with OPP (red) (**g**) with corresponding quantification in (**h**) (n=8, two-sided paired t-test). (**i-j**) Phospho-eIF2α staining (red) in *RpS3*$^{+/-}$ wing discs expressing FOXO in P cells (**i**) and corresponding quantification (n=10, two-sided Wilcoxon signed-rank test. Due to low genetic frequency and the presence of an internal control, samples from multiple experiments were pooled together) (**j**). (**k-l**) Apoptosis detection by cleaved caspase-3 staining (red) in competing wild-type/*RpS3*$^{+/-}$ mosaic wing discs without (**k**) or with (**l**) additional expression of dFOXO specifically in *RpS3*$^{+/-}$ cells. (**m**) Quantification of cell death at *RpS3*$^{+/-}$ clone boundaries for the experiments in (**k-l**) (n=8 and 10, respectively, two-sided two sample Kolmgorov-Smirnov test). For all micrographs, scale bars correspond to 50μm. For all quantifications provided, the horizontal line represents the mean and whiskers indicate 95% confidence intervals. All n numbers refer to the number of individual wing discs.

Figure 6: Proteotoxic stress is sufficient to confer the loser status. (**a-b**) *GstD1*-GFP signal (green) in a wing disc expressing MJDQ78 in P cells (labelled by the absence of Ci, magenta) (**a**) and corresponding quantification (n=8, two-sided Wilcoxon signed-rank test) (**b**). (**c**) GFP-p62 ReFlux signal (green) in wing discs expressing MJDQ78 in P cells, immediately after heat shock or three hours later, as indicated. (**d-e**) p62 staining in a wing disc expressing MJDQ78 in P cells (labelled by the absence of Ci, magenta) (**d**), and corresponding quantification in (**e**) (n=7, two-sided paired t-test). (**f-g**) Wing discs harboring GFP-positive clones expressing MJDQ78 labelled with OPP (red) (**f**) with corresponding quantification relative to wing discs containing competing *RpS3*$^{+/-}$ clones and wildtype winners (image not shown) in (**g**) (n=6 and 7 respectively, two-sided student's t-test). (**h-i**) Mosaic wing disc containing GFP-positive clones overexpressing MJDQ78, immuno-stained for cleaved Caspase-3 (red) (**h**), and corresponding cell death quantification (n= 11, two-sided Wilcoxon signed-rank test) (**i**). (**j-l**) Wing discs harboring wild-type cells and wildtype control clones (GFP-positive) (**k**) or clones expressing MJDQ78 (GFP-positive) (**l**), and corresponding quantification

693 (n=15 and 20 respectively, two-sided Mann-Whitney U test) (**j**). (**m**) Model summarizing
694 how ribosome gene loss leads to proteotoxic stress and to the loser status. For all
695 micrographs, scale bars correspond to 50µm. For all quantifications provided, the
696 horizontal line represents the mean and whiskers indicate 95% confidence intervals. All
697 n numbers refer to the number of individual wing discs.
698
699

Methods

Proteotoxic stress is a driver of the loser status and of cell competition

Michael E. Baumgartner, Michael P. Dinan, Paul F. Langton, Iwo Kucinski, and Eugenia Piddini

Fly husbandry. Fly lines were maintained at 25°C on a flour-based food supplemented with yeast. Our standard recipe contains 7.5g/L agar powder, 50g/L baker's yeast, 55g/L glucose, 35g/L wheat flour, 2.5 % nipagin, 0.4 % propionic acid and 1.0% penicillin/streptomycin. For some chemical feeding experiments, drugs were diluted in Nutrifly GF food (Scientific Laboratory Supplies) made to manufacturer's instructions. Sexes were not differentiated for any experiments, except in cases where transgenes were X-linked. Eggs were collected for 24 hours and wing discs were dissected from wandering third instar larvae. For each dataset, including across different vials or genotypes, egg collections, heat-shocks and harvesting of wandering stage larvae for dissections were done in parallel. All *Drosophila* strains used in this study are provided in Supplemental Table 2, and genotypes for all experimental crosses are provided in Supplemental Table 3.

Immunostaining. Wing discs were dissected in phosphate-buffered saline (PBS) before fixation in 4% formaldehyde/PBS solution for 20 minutes at room temperature. Dissected hemi-larvae were subsequently washed three times in PBS (30 seconds each), before permeabilisation in PBS containing 0.25% Triton X-100 (PBS-T). Samples were next incubated in blocking buffer (PBS-T supplemented with 4% fetal calf serum) for 30 minutes at room temperature. Primary antibodies were diluted in blocking buffer and incubated overnight at 4°C. Samples were washed three times in PBS-T (10 minutes each) before incubation in secondary antibody (diluted in blocking buffer) for 1 hour at room temperature. The secondary antibodies used were conjugated with Alexa 488, Alexa 555 or Alexa 633 dyes (Molecular probes). Nuclei were counterstained with DAPI (0.5 μg/ml). After three 5-minute washes in PBS-T, wing discs were mounted in Vectashield (Vector laboratories) on a borosilicate glass side (no 1.5, VWR international). For anti-FK-2 staining, the blocking buffer was substituted with a 3% BSA in PBS solution. Details and sources of all antibodies are provided in Supplemental Table 2. Dilutions for primary antibodies used are as follows: 1 in 500 for anti-pJNK, 1 in 1000 for anti-Ci, 1 in 2000 for anti-Ref(2)P, 1:25000 for anti-cleaved Caspase-3, 1 in 2500 for anti-DCP1, 1 in 500 for anti-p-eIF2α, and 1 in 5000 for anti-FK2.

Clonal analysis. Mosaic wing discs were generated using the FLP/FRT system employing *hs*-FLP or *en*-Gal4-UAS-FLP transgenic strains. For clone induction, heat shocks were carried out 2-4 days after egg laying (depending on experiment), in a 37°C water bath before returning flies to a 25°C incubator, or for experiments employing a temperature sensitive Gal80 ($Gal80^{TS}$), to a water bath at the indicated temperature. The exact temperature for $Gal80^{TS}$ experiments together with heat shock conditions and clone age, which were optimized for each experiment individually, are listed in Supplemental Table 3.

Translation Assays. AHA and OPP assays were carried out using the Click-iT™ Plus OPP Protein Synthesis Assay kit and Click-iT Plus™ AHA Protein Synthesis Assay kit, respectively. For the AHA assay, wing discs were dissected and inverted in a glass dish before incubation in methionine free Schneider's medium at 25 °C for 45 min. Hemi-larvae were then incubated for a further 45 min in methionine free medium supplemented with 2 mM AHA reagent. Samples were subsequently washed in PBS before fixation in 4% formaldehyde/PBS solution. For OPP assays, larvae were dissected in normal Schneider's medium before transfer to a 1.5 ml Eppendorf containing 5 μM OPP reagent in Schneider's medium and incubation for 15 min at 25 °C. Samples were subsequently washed in PBS before fixation. For both assays, fixed tissues were subsequently stained using the standard Click-iT protocol according to manufacturer's instructions. Details for reagents are provided in Supplemental Table 2.

Identification of proteostasis genes. The full list of genes differentially expressed in *RpS3*$^{+/-}$ cells plus/minus expression of the JNK inhibitor *puc* was reported previously [20]. To identify differentially expressed proteostasis genes from this list we selected genes associated with the following GO terms: autophagy, response to unfolded proteins, proteasome complex, proteasome catabolic process.

Re-Flux and Proteo-Flux Assays. Re-Flux and Proteo-Flux assays were carried out as pulse-chase experiments. Third instar wandering larvae were heat-shocked for 40 to 45

minutes, to induce a pulse of GFP-p62 or CL1-GFP, respectively. Larvae were incubated at 25 degrees for the indicated times to chase protein levels before dissection.

Proteostat assay. For PROTEOSTAT® Protein Aggregation Assay larvae were dissected and inverted in PBS before transfer to a 1.5 ml Eppendorf tube containing 4% formaldehyde diluted in 1X PROTEOSTAT assay buffer (PAB). The samples were subsequently permeabilized in 0.5% Triton X-100, 3 mM EDTA, pH 8.0 diluted in 1X PAB, before staining with PROTEOSTAT detection reagent diluted 1 in 20,000 together with Hoechst 33342 at 1 μg/ml in PAB. Hemi-larvae were subsequently washed three times in PBS before separating wing discs from the larval body and mounting in PBS under our standard cover slips. Wing discs were imaged immediately. Details for reagents are provided in Supplemental Table 2.

Transmission electron microscopy. Larvae were washed and dissected in Schneider's Insect Medium and imaginal wing discs were dissected out and subjected to high-pressure freezing in a 20% BSA solution followed by an osmium tetroxide freeze substitution and Epon embedding. The resulting blocks were sectioned onto grids using an ultramicrotome and stained with uranyl acetate and lead citrate. Sections were then imaged on a Tecnai 12 transmission electron microscope.

Chemical feeding. For bortezomib feeding, eggs were collected for 24 hours and larvae grown on normal food for 72 hours before being floated in a 20% sucrose solution. Floated larvae were thoroughly washed with PBS before transferring to Nutri-Fly™ GF Premixed food containing 10 μM bortezomib or the equivalent volume of DMSO (as a carrier control). Larvae were grown until they were at third instar wandering stages. For rapamycin feeding, 4 μM rapamycin was diluted in standard wheat-based food and floated larvae were maintained on the drug (or equivalent carrier control of ethanol) until wandering stage. For chloroquine incubation, dissected larvae were incubated in 50 μM chloroquine diluted in normal Schneider's medium (or the equivalent

volume of water as a carrier control) for three hours at 25 °C, before washing in PBS and fixation. Details for reagents are provided in Supplemental Table 2.

Proteomics. Third instar larvae raised on normal food were dissected in ice-cold PBS containing 1X Phos-STOP phosphatase inhibitor and 1X Halt Protease Inhibitor cocktail. Wing discs were then centrifugated in an Eppendorf containing PBS/inhibitor cocktail for 30 seconds at 6,000 rcf at 4 °C before being lysed in ice-cold RIPA lysis buffer. Lysed samples were centrifugated at 12,500 rcf at 4 °C for ten minutes. Aliquots of 50µg of each sample were digested with trypsin (1.25µg trypsin; 37°C, overnight), and labelled with Tandem Mass Tag (TMT) ten plex reagents according to the manufacturer's protocol (Thermo Fisher Scientific, Loughborough, LE11 5RG, UK) before samples were pooled. 40ug of the pooled sample was desalted using a SepPak cartridge according to the manufacturer's instructions (Waters, Milford, Massachusetts, USA). Eluate from the SepPak cartridge was evaporated to dryness and resuspended in buffer A (20 mM ammonium hydroxide, pH 10) prior to fractionation by high pH reversed-phase chromatography using an Ultimate 3000 liquid chromatography system (Thermo Fisher Scientific). In brief, the sample was loaded onto an XBridge BEH C18 Column (130Å, 3.5 µm, 2.1 mm X 150 mm, Waters, UK) in buffer A and peptides eluted with an increasing gradient of buffer B (20 mM Ammonium Hydroxide in acetonitrile, pH 10) from 0-95% over 60 minutes. The resulting fractions were evaporated to dryness and resuspended in 1% formic acid prior to analysis by nano-LC MSMS using an Orbitrap Fusion Lumos mass spectrometer (Thermo Scientific).

High pH reversed-phase fractions were further fractionated using an Ultimate 3000 nano-LC system in line with an Orbitrap Fusion Lumos mass spectrometer (Thermo Scientific). All spectra were acquired using an Orbitrap Fusion Lumos mass spectrometer controlled by Xcalibur 3.0 software (Thermo Scientific) and operated in data-dependent acquisition mode using an SPS-MS3 workflow. FTMS1 spectra were collected at a resolution of 120 000, with an automatic gain control (AGC) target of 400 000 and a max injection time of 100ms. Precursors were filtered with an intensity threshold of 5000, according to charge state (to include charge states 2-7) and with

monoisotopic peak determination set to Peptide. Previously interrogated precursors were excluded using a dynamic window (60s +/-10ppm). The MS2 precursors were isolated with a quadrupole isolation window of 0.7m/z. ITMS2 spectra were collected with an AGC target of 10 000, max injection time of 70ms and CID collision energy of 35%.

For FTMS3 analysis, the Orbitrap was operated at 30 000 resolution with an AGC target of 50 000 and a max injection time of 105ms. Precursors were fragmented by high energy collision dissociation (HCD) at a normalised collision energy of 60% to ensure maximal TMT reporter ion yield. Synchronous Precursor Selection (SPS) was enabled to include up to 5 MS2 fragment ions in the FTMS3 scan.

The raw data files were processed and quantified using Proteome Discoverer software v2.1 (Thermo Scientific) and searched against the UniProt Drosophila melanogaster database (downloaded March 2020: 41311 entries) using the SEQUEST HT algorithm. Peptide precursor mass tolerance was set at 10ppm, and MS/MS tolerance was set at 0.6Da. Searches were performed with full tryptic digestion and a maximum of 2 missed cleavages were allowed. The reverse database search option was enabled and all data was filtered to satisfy false discovery rate (FDR) of 5%. Ribosomal proteins were identified by cross referencing the proteomic results against the 'Ribosomal Protein' category in FlyBase using R statistical software. Average fold changes were obtained for Ribosomal Proteins which exhibited a consistent change in relative abundance across both biological replicates. Two biological replicates were performed.

Cloning and transgenics. To isolate genomic DNA, a single fly was homogenized in 50 μl extraction buffer containing 10 mM Tris HCl pH 8.2, 2 mM EDTA pH 8.0, 0.1% Triton X-100 and 200 μg/ml proteinase K. Samples were then heated to 55 °C for 30 min in a Thermoshaker with occasional vortexing, before increasing the temperature to 95 °C for 15 min to inhibit protease activity. Samples were then cooled to 4 °C and centrifuged at 5,000 x g for 5 min at 4 °C. The supernatant was subsequently transferred to a fresh 0.5 ml Eppendorf tube and stored at 4 °C. Alternatively, DNA was

isolated from 10-15 flies using a Gentra Puregene Tissue Kit using the following protocol: flies were homogenized using a motorized pestle in 200 μl cell lysis buffer and incubated at 65 °C in a Thermoshaker for 15 min. Then, 1 μl RNAase A solution was added, before incubation at 37 °C for a further 15 min. A volume of 100 μl of protein precipitation buffer was subsequently added and samples were thoroughly mixed and incubated on ice for 5 min. Samples were centrifuged for 10 min at 4 °C, at max speed before adding 300 μl isopropanol to the supernatant, mixing well and a further 15 min in the centrifuge. The resulting pellet was washed twice with 70 % ethanol before re-suspending in 50 μl of DNAse free water.

For cloning of both ReFLUX (hs-GFP-p62) and ProteoFLUX (hs-CL1-GFP) constructs, gDNA was isolated from 10-15 flies of the genotypes *UAS-GFP-p62* or *UAS-CL1-GFP* respectively. The resulting gDNA was used as template for a PCR using primers designed to amplify constructs introduced in the common pUAST vector. To generate pCaSper-hs-GFP-p62 three different pairs of primers were used to generate a PCR product that could be inserted into the pCR™4-TOPO™ vector. The resulting pTOPO-GFP-p62 together with pCaSper-hs were digested with XbaI and NotI restriction enzymes (New England Biosciences Ltd) to produce a fragment containing GFP-p62 that could be ligated into the pCaSper-hs backbone. For the hs-CL1-GFP, a protocol using Infusion® HD Cloning Plus Kit was designed to infuse a PCR product containing the CL1-GFP sequencing into the pCasper-hs-GFP-p62 plasmid.

For cloning of the *act>RpS3>Gal4* construct, the Infusion® HD Cloning Plus Kit (Clontech, 638909) was used to linearize an extant pCaSper2-act>CD2>Gal4 vector [64], by digestion with the *Acc65I* restriction enzyme (NEB). Two PCR products from a plasmid encoding *RpS3* together with *Hsp70* terminator sequences, were then infused. The resulting plasmid was transformed into Stellar™ competent cells (Clontech, 636766).

Plasmids for all constructs were sent for injection into a *w118* line by Genetics Services, University of Cambridge or BestGene *Drosophila* embryo injection services. Exact primers used are provided in Supplemental Table 2.

Image acquisition and processing. Confocal images were acquired using Leica SP5 and SP8 confocal microscopes using a 40x 1.3 NA P Apo Oil objective. All wing discs were imaged as z-stacks with each section corresponding to 0.5-1 μm. Images were subsequently analysed and processed using Fiji2 and Photoshop (Adobe Version CS6). Clonal areas were determined using a custom script built in Fiji. For cell death quantifications, caspase-3 or DCP1 positive cells were counted in the region specified in each experiment (as reported in the figure legend). All counts were normalized to their respective area as measured in Fiji. For signal intensity, mean grey value was measured in Fiji for the specified genotypes within the pouch region of the wing disc.

Quantifications. For immunofluorescence and fluorescent reporter microscopy-based assays, all measurements were derived from the pouch region of the wing disc. For cell death assays, death counts were normalized to the area of the wing pouch or to the specified region of the clones within the pouch. For all scatter dot plots, unless otherwise specified, the horizontal line represents the mean and whiskers indicate 95% confidence intervals.

Statistics and reproducibility. All data used for statistical tests along with the specific test used for each experiment are shown in the Statistics Source Data table. Statistical tests were performed using GraphPad Prism 7.0a and Rstudio software. P-values were determined using univariate statistics. We consider not significant (n.s.) p-values >0.05. Parametric tests were used in cases where assumptions of normality and equivalence of variance were met. Non-parametric tests were used otherwise. The parametric tests used were Student's T-Test and paired T-Test for matched data. The non-parametric tests used were either a Kolmogorov-Smirnov test or Mann Whitney U-test, or Wilcoxon matched-pairs signed rank test for matched data. P-value corrections for multiple comparisons were not considered due to the low number of comparisons. All statistical

tests were two-sided. A minimum of three biological repeats were used for experiments comparing across separate wing discs. For matched experiments containing an internal control, a minimum of two biological repeats were performed. Functional validation of reagents and *Drosophila* stocks (e.g. RNAi) was carried out at least once. All data points for all replicates for specific quantifications are provided in the 'Statistics Source Data' supplemental file.

Code availability: The Fiji-based custom-made script can be made available to individuals upon reasonable request, while we seek to publish it independently of this study.

Data availability: All source numerical data are provided in the Statistics Source Data table. All other data supporting the findings of this study are available upon reasonable request. The following publicly available databases were used in this study: Flybase (https://flybase.org); Uniprot D. melanogaster proteome (https://www.uniprot.org/proteomes/UP000000803).

References

64. Zhou, Q., Neal, S. J. & Pignoni, F. Mutant analysis by rescue gene excision: New tools for mosaic studies in Drosophila. *Genesis* **54,** 589–592 (2016).
65. Katheder, N. S. *et al.* Microenvironmental autophagy promotes tumour growth. *Nature* **541,** 417–420 (2017).
66. Gay, P. & Contamine, D. Study of the ref(2)P locus of Drosophila melanogaster. II. Genetic studies of the 37DF region. *Mol. Gen. Genet.* **239,** 361–370 (1993).

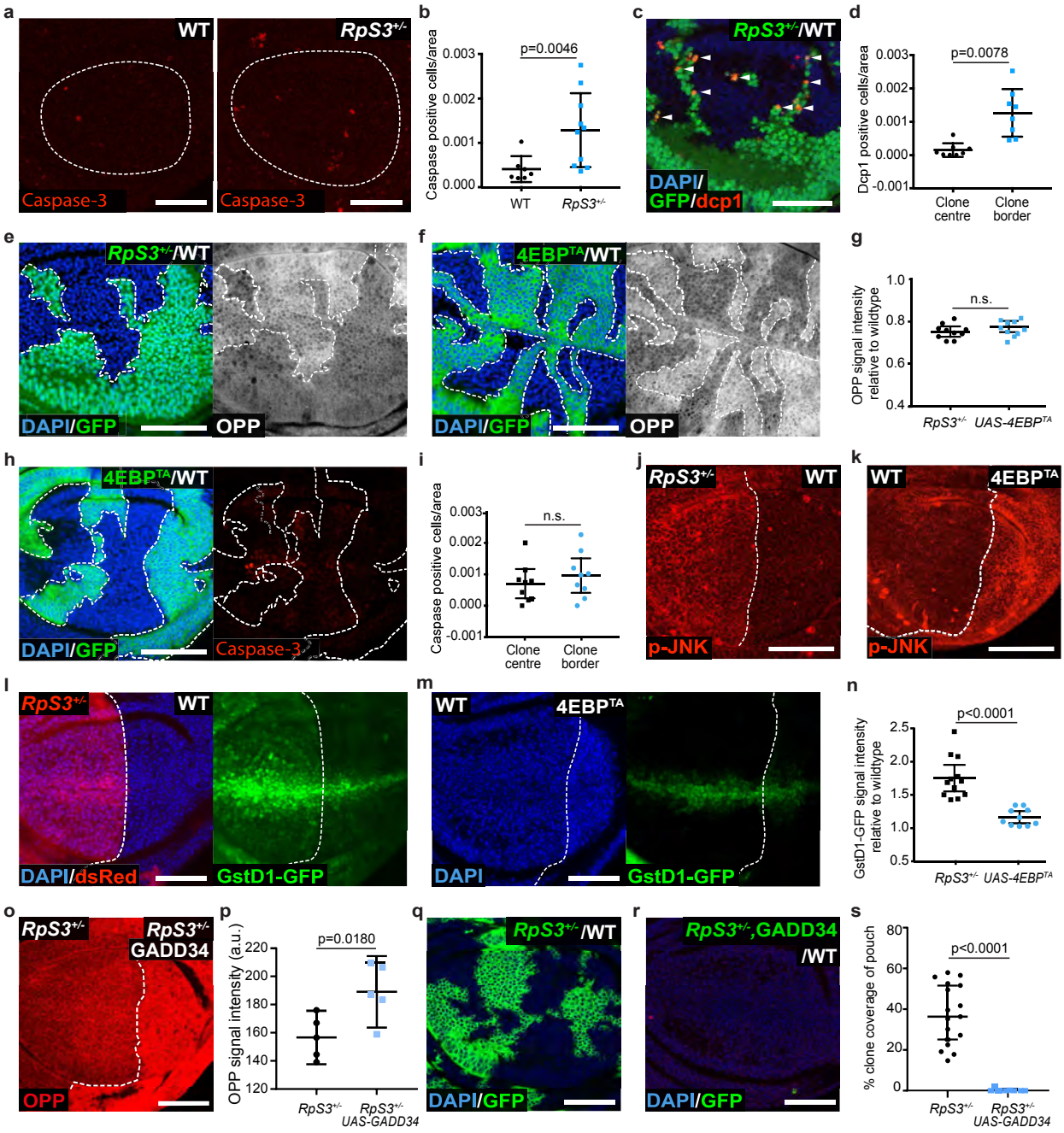
a
WT
RpS3+/-
Caspase-3
Caspase-3
b
Caspase positive cells/area
0.003
0.002
0.001
0.000
p=0.0046
WT
RpS3+/-
c
RpS3+/-/WT
DAPI/
GFP/dcp1
d
Dcp1 positive cells/area
0.003
0.002
0.001
0.000
-0.001
p=0.0078
Clone centre
Clone border
e
RpS3+/-/WT
DAPI/GFP
OPP
f
4EBPTA/WT
DAPI/GFP
OPP
g
OPP signal intensity relative to wildtype
1.0
0.8
0.6
0.4
n.s.
RpS3+/-
UAS-4EBPTA
h
4EBPTA/WT
DAPI/GFP
Caspase-3
i
Caspase positive cells/area
0.003
0.002
0.001
0.000
-0.001
n.s.
Clone centre
Clone border
j
RpS3+/-
WT
p-JNK
k
WT
4EBPTA
p-JNK
l
RpS3+/-
WT
DAPI/dsRed
GstD1-GFP
m
WT
4EBPTA
DAPI
GstD1-GFP
n
GstD1-GFP signal intensity relative to wildtype
2.5
2.0
1.5
1.0
0.5
p<0.0001
RpS3+/-
UAS-4EBPTA
o
RpS3+/-
RpS3+/-
GADD34
OPP
p
OPP signal intensity (a.u.)
220
200
180
160
140
120
p=0.0180
RpS3+/-
RpS3+/-
UAS-GADD34
q
RpS3+/-/WT
DAPI/GFP
r
RpS3+/-,GADD34
/WT
DAPI/GFP
s
% clone coverage of pouch
80
60
40
20
0
p<0.0001
RpS3+/-
RpS3+/-
UAS-GADD34

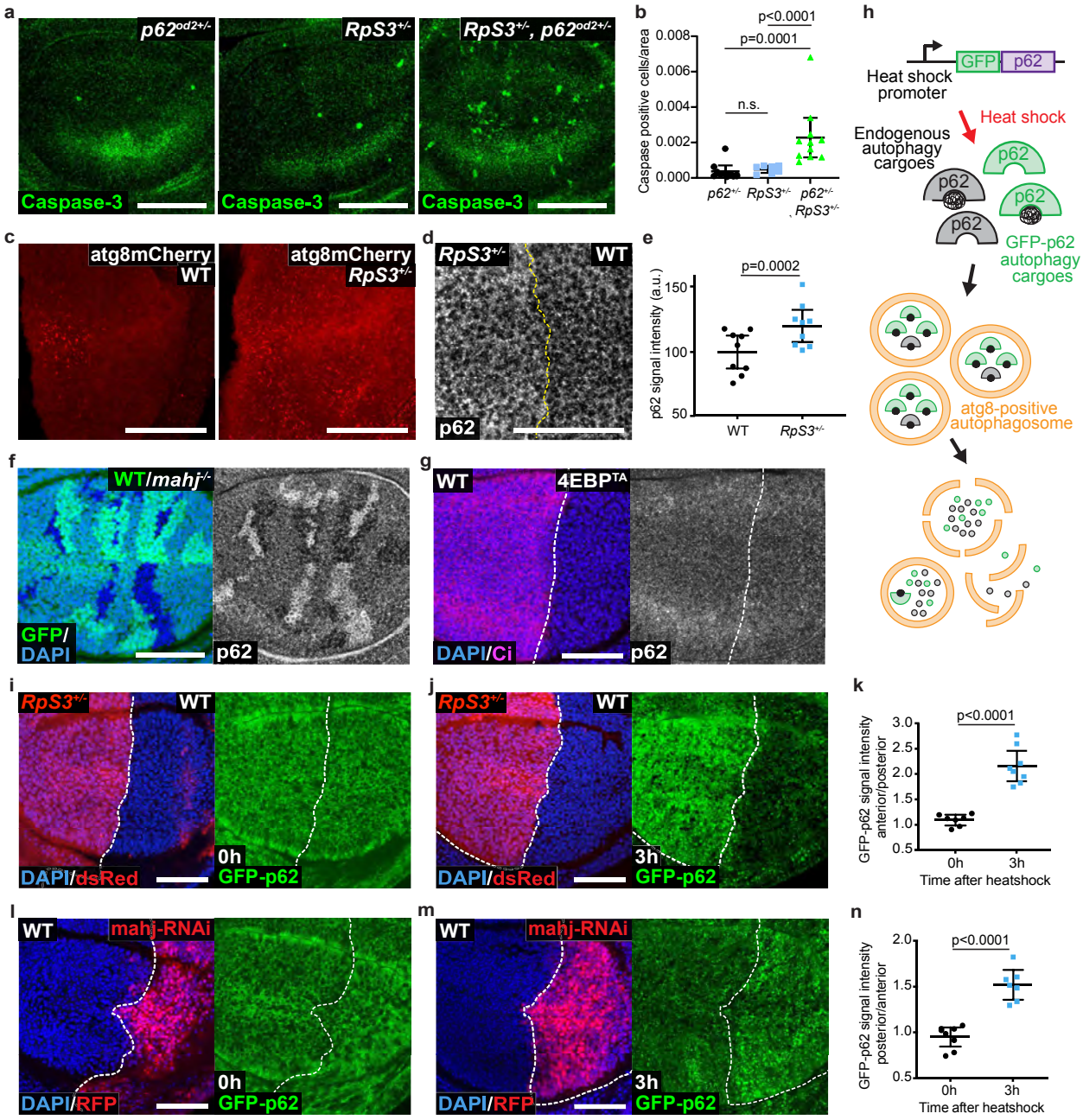
a
p62od2+/-
RpS3+/-
RpS3+/-, p62od2+/-
Caspase-3
Caspase-3
Caspase-3
b
p<0.0001
p=0.0001
n.s.
Caspase positive cells/area
0.008
0.006
0.004
0.002
0.000
p62+/-
RpS3+/-
p62+/- RpS3+/-
h
Heat shock promoter
GFP
p62
Heat shock
Endogenous autophagy cargoes
p62
p62
p62
GFP-p62 autophagy cargoes
atg8-positive autophagosome
c
atg8mCherry WT
atg8mCherry RpS3+/-
d
RpS3+/-
WT
p62
e
p=0.0002
p62 signal intensity (a.u.)
150
100
50
WT
RpS3+/-
f
WT/mahj-/-
GFP/ DAPI
p62
g
WT
4EBPTA
DAPI/Ci
p62
i
RpS3+/-
WT
DAPI/dsRed
0h
GFP-p62
j
RpS3+/-
WT
DAPI/dsRed
3h
GFP-p62
k
p<0.0001
GFP-p62 signal intensity anterior/posterior
3.0
2.5
2.0
1.5
1.0
0.5
0h
3h
Time after heatshock
l
WT
mahj-RNAi
DAPI/RFP
0h
GFP-p62
m
WT
mahj-RNAi
DAPI/RFP
3h
GFP-p62
n
p<0.0001
GFP-p62 signal intensity posterior/anterior
2.0
1.5
1.0
0.5
0h
3h
Time after heatshock

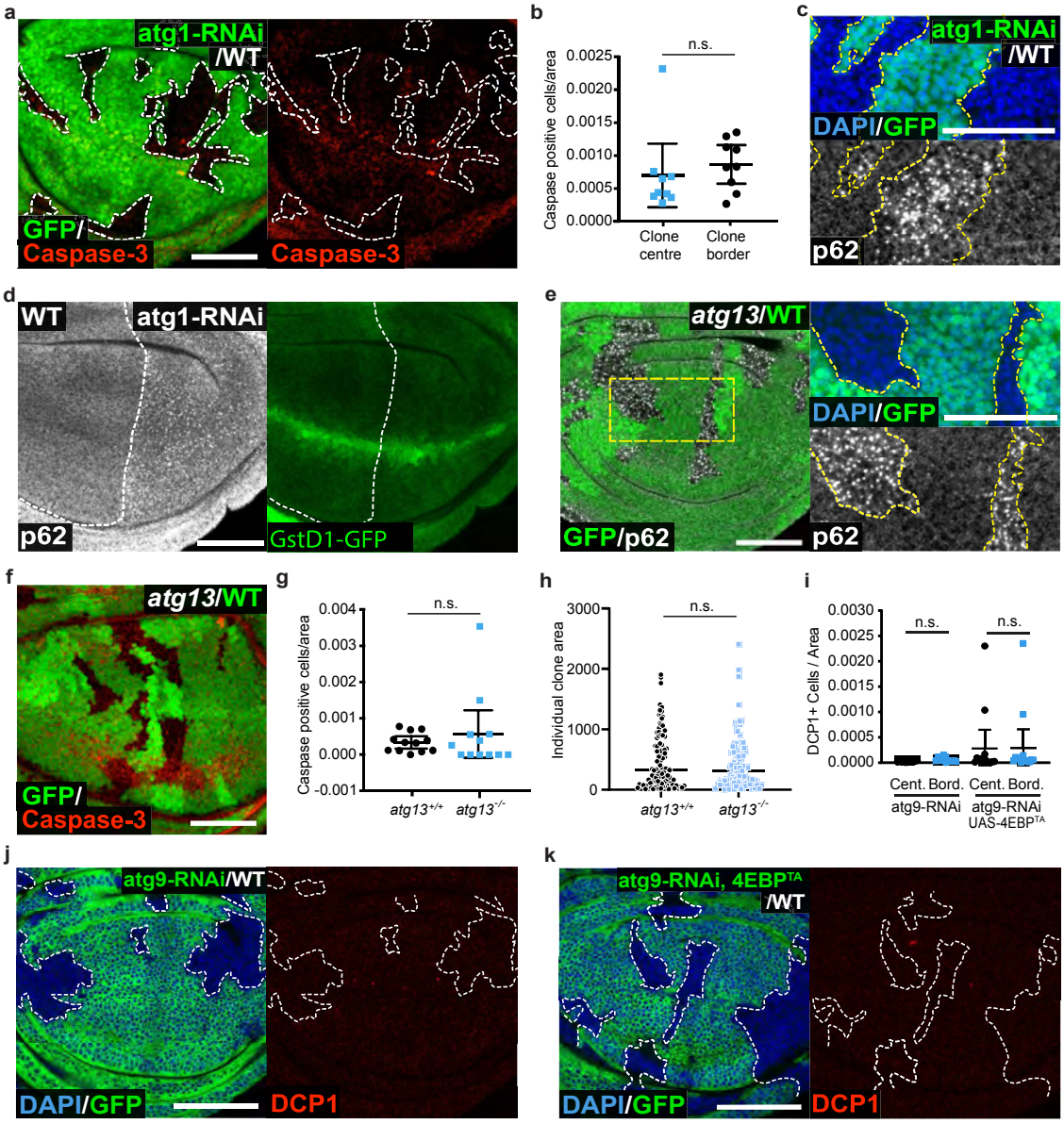
a
atg1-RNAi
/WT
GFP/
Caspase-3
Caspase-3
b
n.s.
Caspase positive cells/area
0.0025
0.0020
0.0015
0.0010
0.0005
0.0000
Clone centre
Clone border
c
atg1-RNAi
/WT
DAPI/GFP
p62
d
WT
atg1-RNAi
p62
GstD1-GFP
e
atg13/WT
DAPI/GFP
GFP/p62
p62
f
atg13/WT
GFP/
Caspase-3
g
n.s.
Caspase positive cells/area
0.004
0.003
0.002
0.001
0.000
-0.001
atg13+/+
atg13-/-
h
n.s.
Individual clone area
3000
2000
1000
0
atg13+/+
atg13-/-
i
n.s.
n.s.
DCP1+ Cells / Area
0.0030
0.0025
0.0020
0.0015
0.0010
0.0005
0.0000
Cent.
Bord.
Cent.
Bord.
atg9-RNAi
atg9-RNAi
UAS-4EBPTA
j
atg9-RNAi/WT
DAPI/GFP
DCP1
k
atg9-RNAi, 4EBPTA
/WT
DAPI/GFP
DCP1

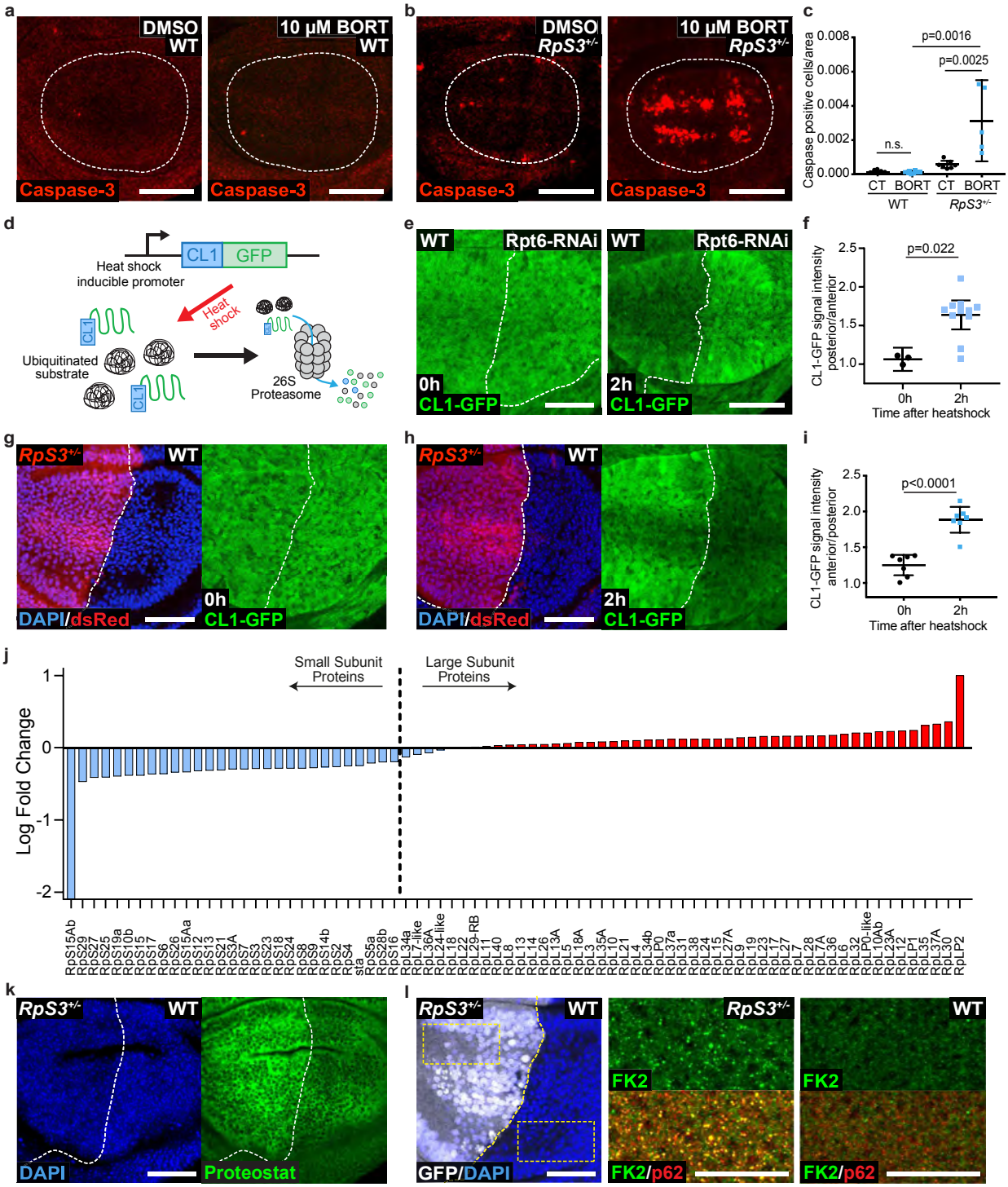
a
DMSO
WT
10 μM BORT
WT
Caspase-3
Caspase-3
b
DMSO
RpS3+/-
10 μM BORT
RpS3+/-
Caspase-3
Caspase-3
c
Caspase positive cells/area
0.008
0.006
0.004
0.002
0.000
p=0.0016
p=0.0025
n.s.
CT
BORT
CT
BORT
WT
RpS3+/-
d
Heat shock
inducible promoter
CL1
GFP
Heat shock
Ubiquitinated
substrate
26S
Proteasome
e
WT
Rpt6-RNAi
WT
Rpt6-RNAi
0h
CL1-GFP
2h
CL1-GFP
f
CL1-GFP signal intensity
posterior/anterior
2.5
2.0
1.5
1.0
p=0.022
0h
2h
Time after heatshock
g
RpS3+/-
WT
DAPI/dsRed
0h
CL1-GFP
h
RpS3+/-
WT
DAPI/dsRed
2h
CL1-GFP
i
CL1-GFP signal intensity
anterior/posterior
2.5
2.0
1.5
1.0
p<0.0001
0h
2h
Time after heatshock
j
Small Subunit
Proteins
Large Subunit
Proteins
Log Fold Change
1
0
-1
-2
RpS15Ab
RpS29
RpS27
RpS25
RpS19a
RpS10b
RpS15
RpS17
RpS6
RpS26
RpS15Aa
RpS12
RpS13
RpS21
RpS3A
RpS7
RpS3
RpS23
RpS18
RpS24
RpS8
RpS9
RpS14b
RpS2
RpS4
sta
RpS5a
RpS28b
RpS16
RpL34a
RpL7-like
RpL36A
RpL24-like
RpL18
RpL22
RpL29-RB
RpL11
RpL40
RpL8
RpL13
RpL14
RpL26
RpL13A
RpL5
RpL18A
RpL3
RpL35A
RpL10
RpL21
RpL4
RpL34b
RpLP0
RpL37a
RpL31
RpL38
RpL24
RpL15
RpL27A
RpL9
RpL19
RpL23
RpL17
RpL27
RpL7
RpL28
RpL7A
RpL36
RpL32
RpLP0-like
RpL10Ab
RpL23A
RpL12
RpLP1
RpL35
RpL37A
RpL30
RpLP2
k
RpS3+/-
WT
DAPI
Proteostat
l
RpS3+/-
WT
GFP/DAPI
RpS3+/-
FK2
FK2/p62
WT
FK2
FK2/p62

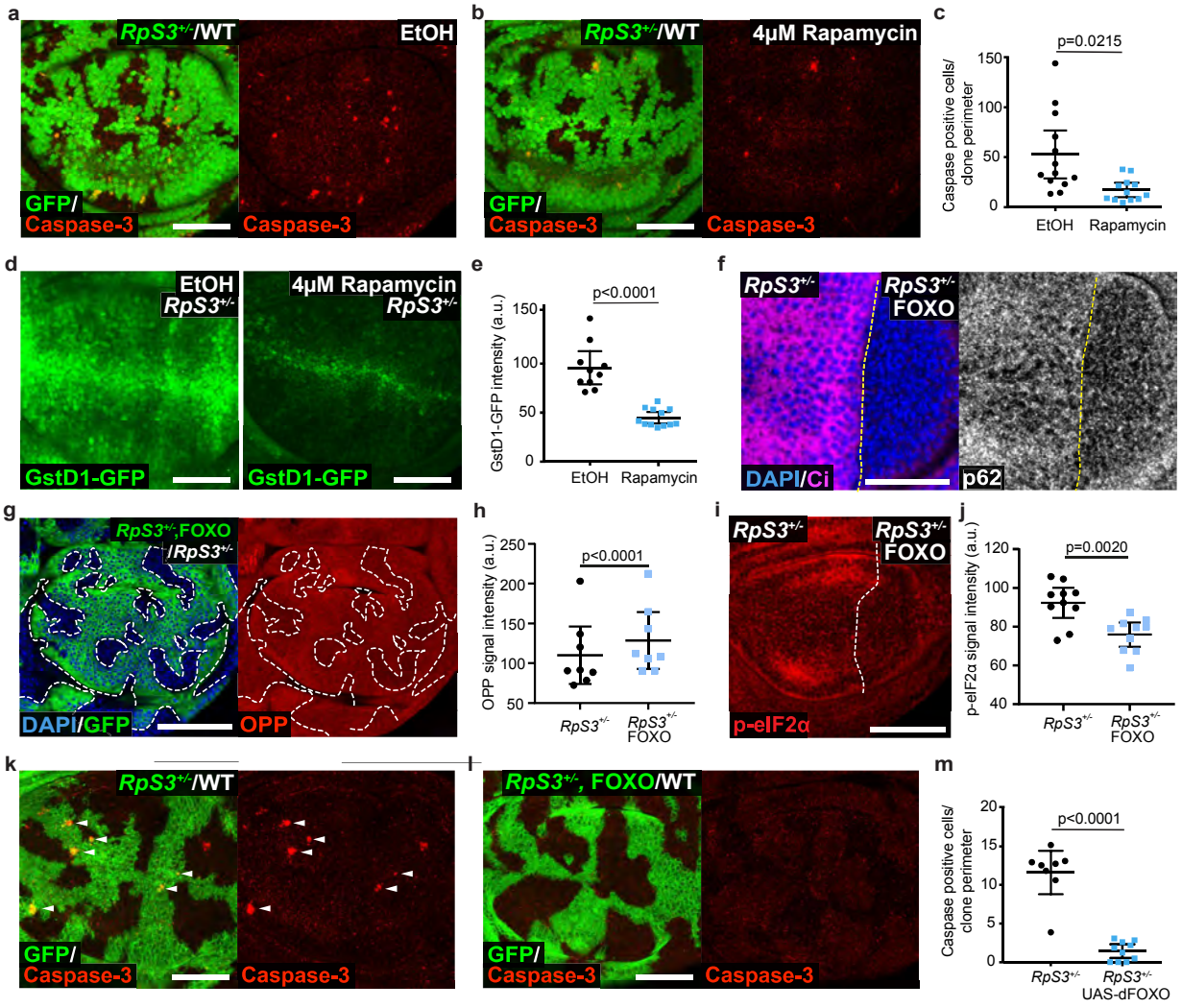
a
RpS3+/-/WT
EtOH
GFP/
Caspase-3
Caspase-3
b
RpS3+/-/WT
4μM Rapamycin
GFP/
Caspase-3
Caspase-3
c
p=0.0215
Caspase positive cells/ clone perimeter
150
100
50
0
EtOH
Rapamycin
d
EtOH
RpS3+/-
4μM Rapamycin
RpS3+/-
GstD1-GFP
GstD1-GFP
e
p<0.0001
GstD1-GFP intensity (a.u.)
150
100
50
0
EtOH
Rapamycin
f
RpS3+/-
RpS3+/-
FOXO
DAPI/Ci
p62
g
RpS3+/-FOXO
/RpS3+/-
DAPI/GFP
OPP
h
p<0.0001
OPP signal intensity (a.u.)
250
200
150
100
50
RpS3+/-
RpS3+/-
FOXO
i
RpS3+/-
RpS3+/-
FOXO
p-eIF2α
j
p=0.0020
p-eIF2α signal intensity (a.u.)
120
100
80
60
40
RpS3+/-
RpS3+/-
FOXO
k
RpS3+/-/WT
GFP/
Caspase-3
Caspase-3
l
RpS3+/-, FOXO/WT
GFP/
Caspase-3
Caspase-3
m
p<0.0001
Caspase positive cells/ clone perimeter
20
15
10
5
0
RpS3+/-
RpS3+/-
UAS-dFOXO

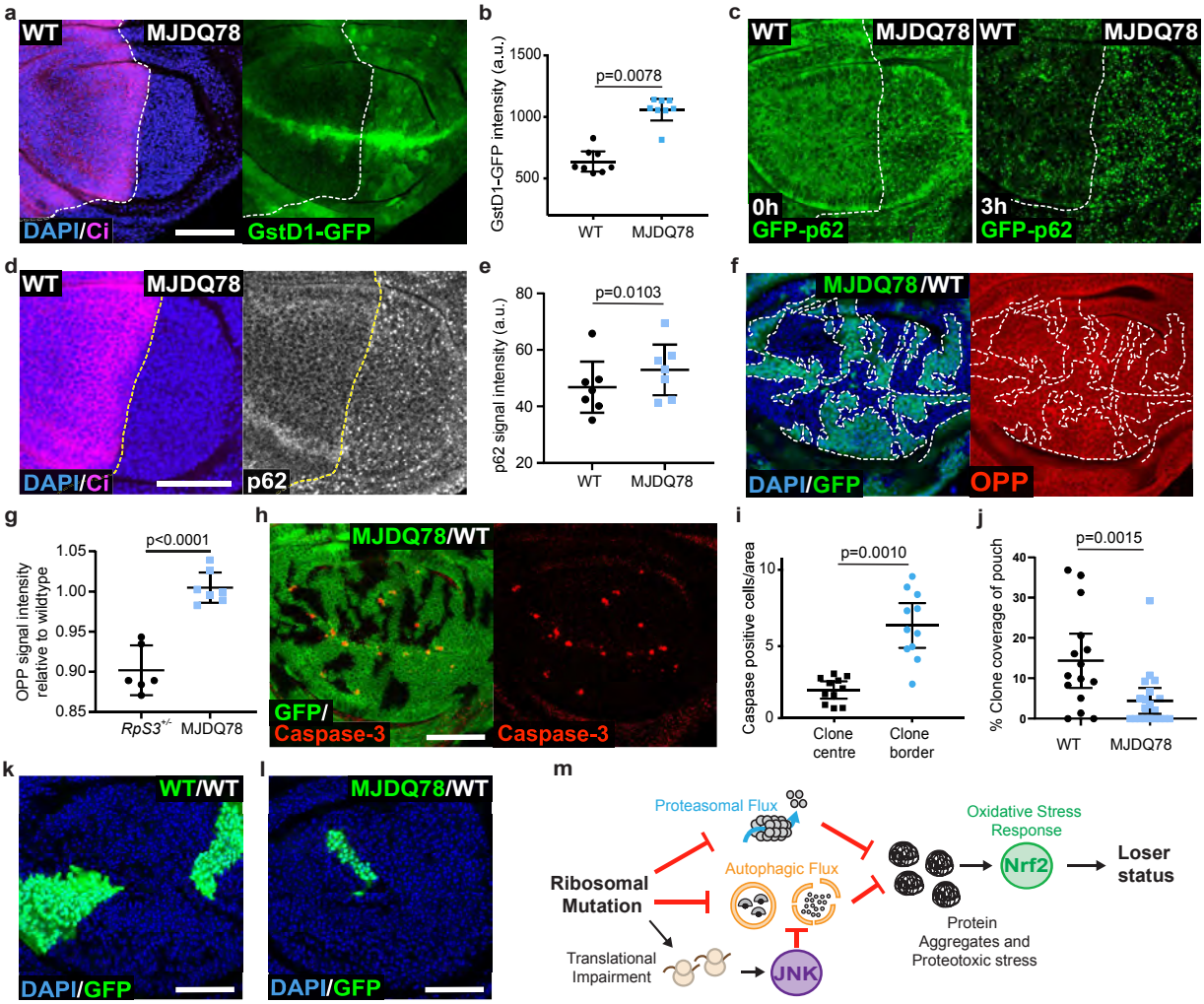
a
WT
MJDQ78
DAPI/Ci
GstD1-GFP
b
GstD1-GFP intensity (a.u.)
1500
1000
500
p=0.0078
WT
MJDQ78
c
WT
MJDQ78
0h
GFP-p62
WT
MJDQ78
3h
GFP-p62
d
WT
MJDQ78
DAPI/Ci
p62
e
p62 signal intensity (a.u.)
80
60
40
20
p=0.0103
WT
MJDQ78
f
MJDQ78/WT
DAPI/GFP
OPP
g
OPP signal intensity relative to wildtype
1.05
1.00
0.95
0.90
0.85
p<0.0001
RpS3+/-
MJDQ78
h
MJDQ78/WT
GFP/
Caspase-3
Caspase-3
i
Caspase positive cells/area
10
5
0
p=0.0010
Clone centre
Clone border
j
% Clone coverage of pouch
40
30
20
10
0
p=0.0015
WT
MJDQ78
k
WT/WT
DAPI/GFP
l
MJDQ78/WT
DAPI/GFP
m
Proteasomal Flux
Autophagic Flux
Ribosomal Mutation
Translational Impairment
JNK
Oxidative Stress Response
Nrf2
Loser status
Protein Aggregates and Proteotoxic stress

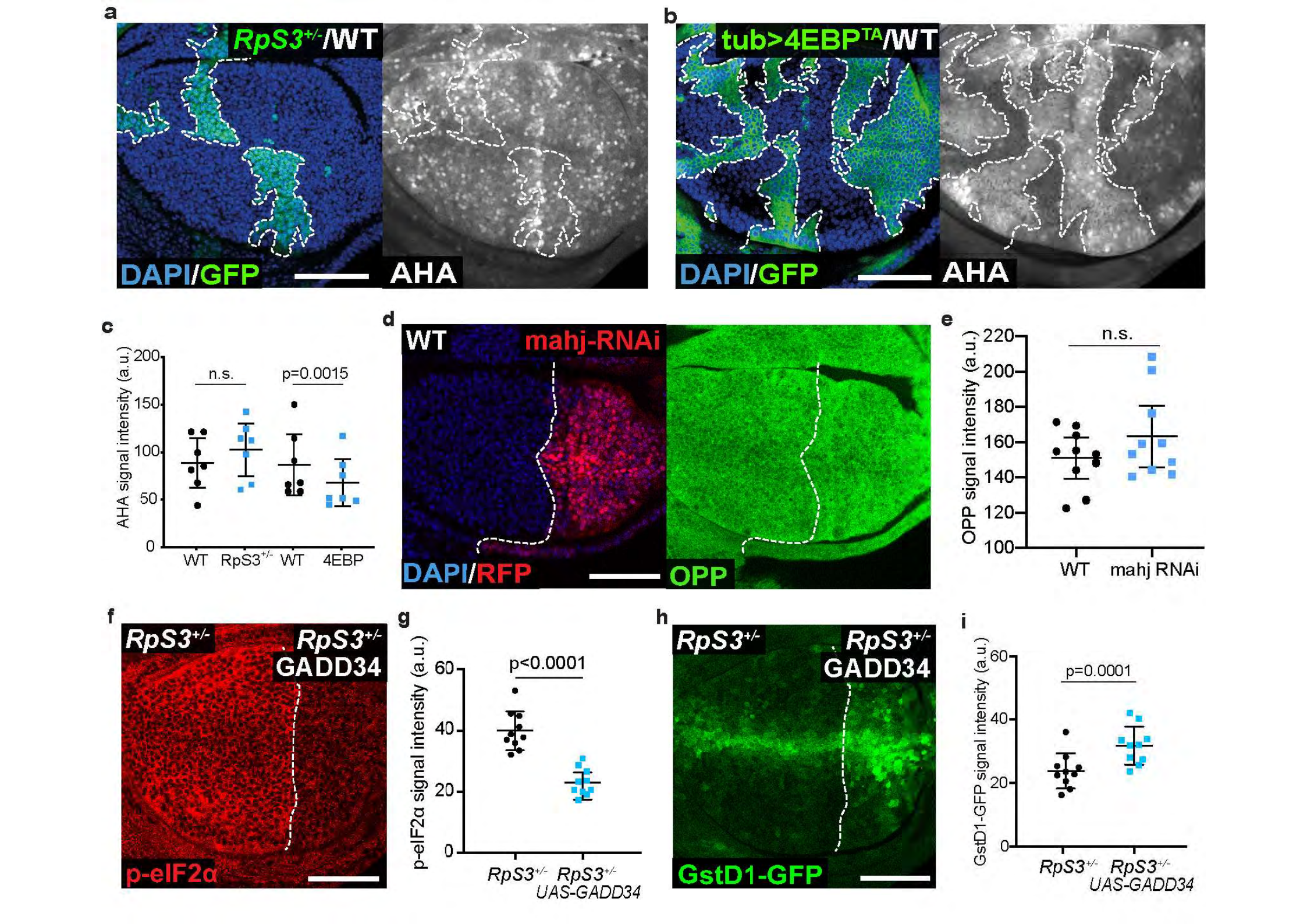
a
RpS3+/-/WT
DAPI/GFP
AHA
b
tub>4EBPTA/WT
DAPI/GFP
AHA
c
AHA signal intensity (a.u.)
200
150
100
50
0
n.s.
p=0.0015
WT
RpS3+/-
WT
4EBP
d
WT
mahj-RNAi
DAPI/RFP
OPP
e
OPP signal intensity (a.u.)
220
200
180
160
140
120
100
n.s.
WT
mahj RNAi
f
RpS3+/-
RpS3+/-
GADD34
p-eIF2α
g
p-eIF2α signal intensity (a.u.)
60
40
20
0
p<0.0001
RpS3+/-
RpS3+/-
UAS-GADD34
h
RpS3+/-
RpS3+/-
GADD34
GstD1-GFP
i
GstD1-GFP signal intensity (a.u.)
60
40
20
0
p=0.0001
RpS3+/-
RpS3+/-
UAS-GADD34

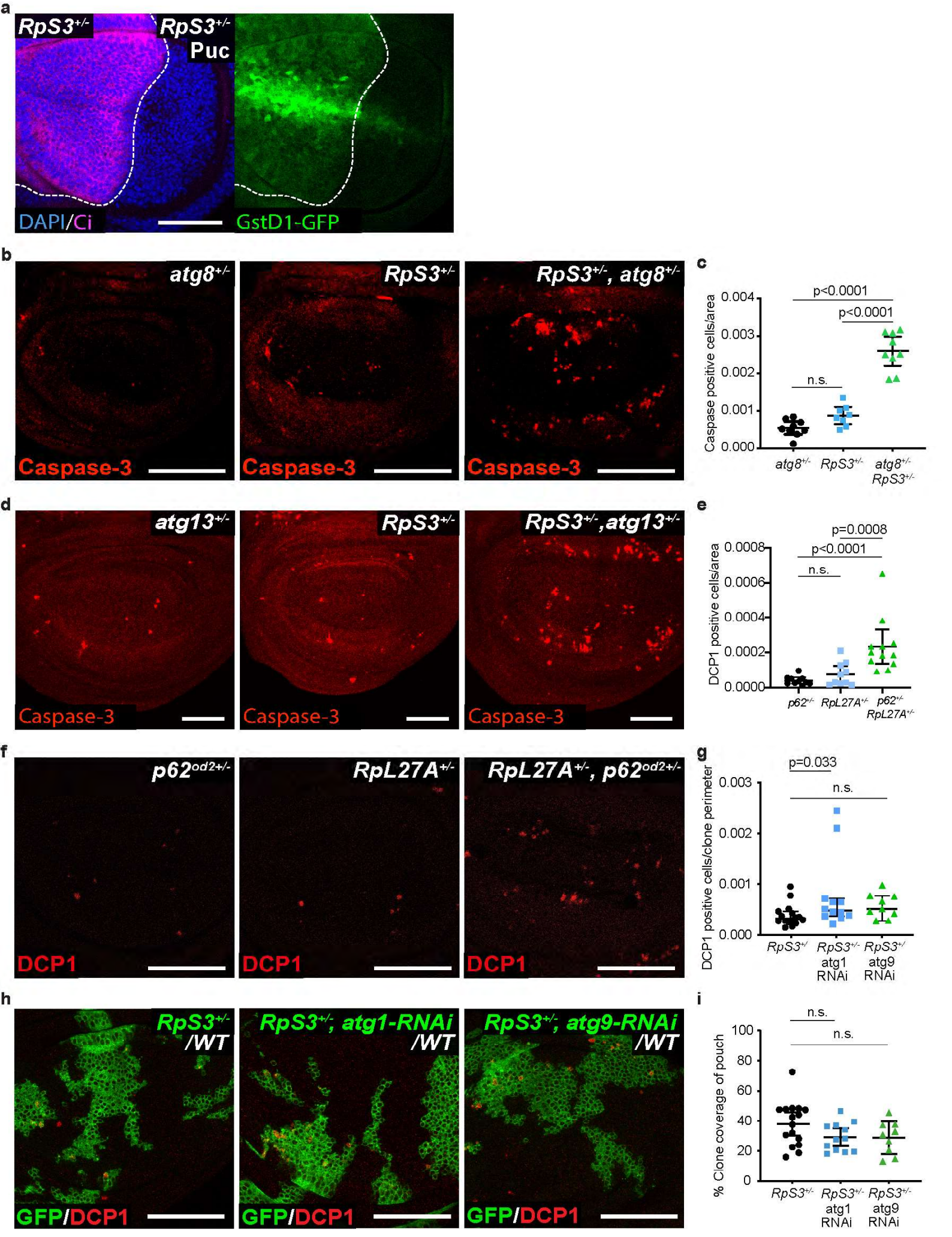
a
RpS3+/-
RpS3+/-
Puc
DAPI/Ci
GstD1-GFP
b
atg8+/-
RpS3+/-
RpS3+/-, atg8+/-
Caspase-3
Caspase-3
Caspase-3
c
Caspase positive cells/area
0.004
0.003
0.002
0.001
0.000
p<0.0001
p<0.0001
n.s.
atg8+/-
RpS3+/-
atg8+/- RpS3+/-
d
atg13+/-
RpS3+/-
RpS3+/-,atg13+/-
Caspase-3
Caspase-3
Caspase-3
e
DCP1 positive cells/area
0.0008
0.0006
0.0004
0.0002
0.0000
p=0.0008
p<0.0001
n.s.
p62+/-
RpL27A+/-
p62+/- RpL27A+/-
f
p62od2+/-
RpL27A+/-
RpL27A+/-, p62od2+/-
DCP1
DCP1
DCP1
g
DCP1 positive cells/clone perimeter
0.003
0.002
0.001
0.000
p=0.033
n.s.
RpS3+/-
RpS3+/- atg1 RNAi
RpS3+/- atg9 RNAi
h
RpS3+/- /WT
RpS3+/-; atg1-RNAi /WT
RpS3+/-; atg9-RNAi /WT
GFP/DCP1
GFP/DCP1
GFP/DCP1
i
% Clone coverage of pouch
100
80
60
40
20
0
n.s.
n.s.
RpS3+/-
RpS3+/- atg1 RNAi
RpS3+/- atg9 RNAi

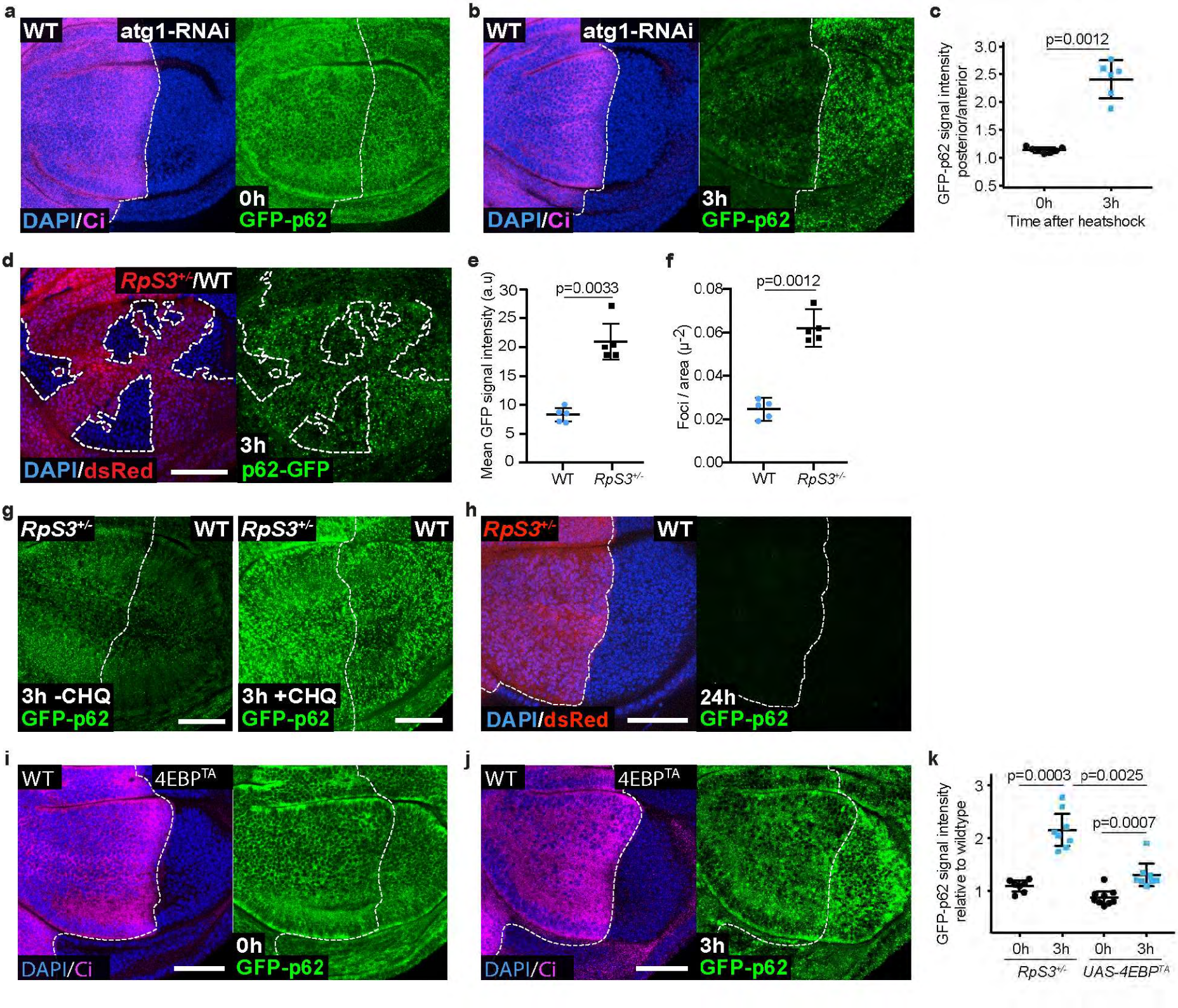
a
WT
atg1-RNAi
DAPI/Ci
0h
GFP-p62
b
WT
atg1-RNAi
DAPI/Ci
3h
GFP-p62
c
p=0.0012
GFP-p62 signal intensity posterior/anterior
3.0
2.5
2.0
1.5
1.0
0.5
0h
3h
Time after heatshock
d
RpS3+/-/WT
DAPI/dsRed
3h
p62-GFP
e
p=0.0033
Mean GFP signal intensity (a.u)
30
25
20
15
10
5
0
WT
RpS3+/-
f
p=0.0012
Foci / area (µ-2)
0.08
0.06
0.04
0.02
0.00
WT
RpS3+/-
g
RpS3+/-
WT
3h -CHQ
GFP-p62
RpS3+/-
WT
3h +CHQ
GFP-p62
h
RpS3+/-
WT
DAPI/dsRed
24h
GFP-p62
i
WT
4EBPTA
DAPI/Ci
0h
GFP-p62
j
WT
4EBPTA
DAPI/Ci
3h
GFP-p62
k
p=0.0003
p=0.0025
p=0.0007
GFP-p62 signal intensity relative to wildtype
3
2
1
0h
3h
0h
3h
RpS3+/-
UAS-4EBPTA

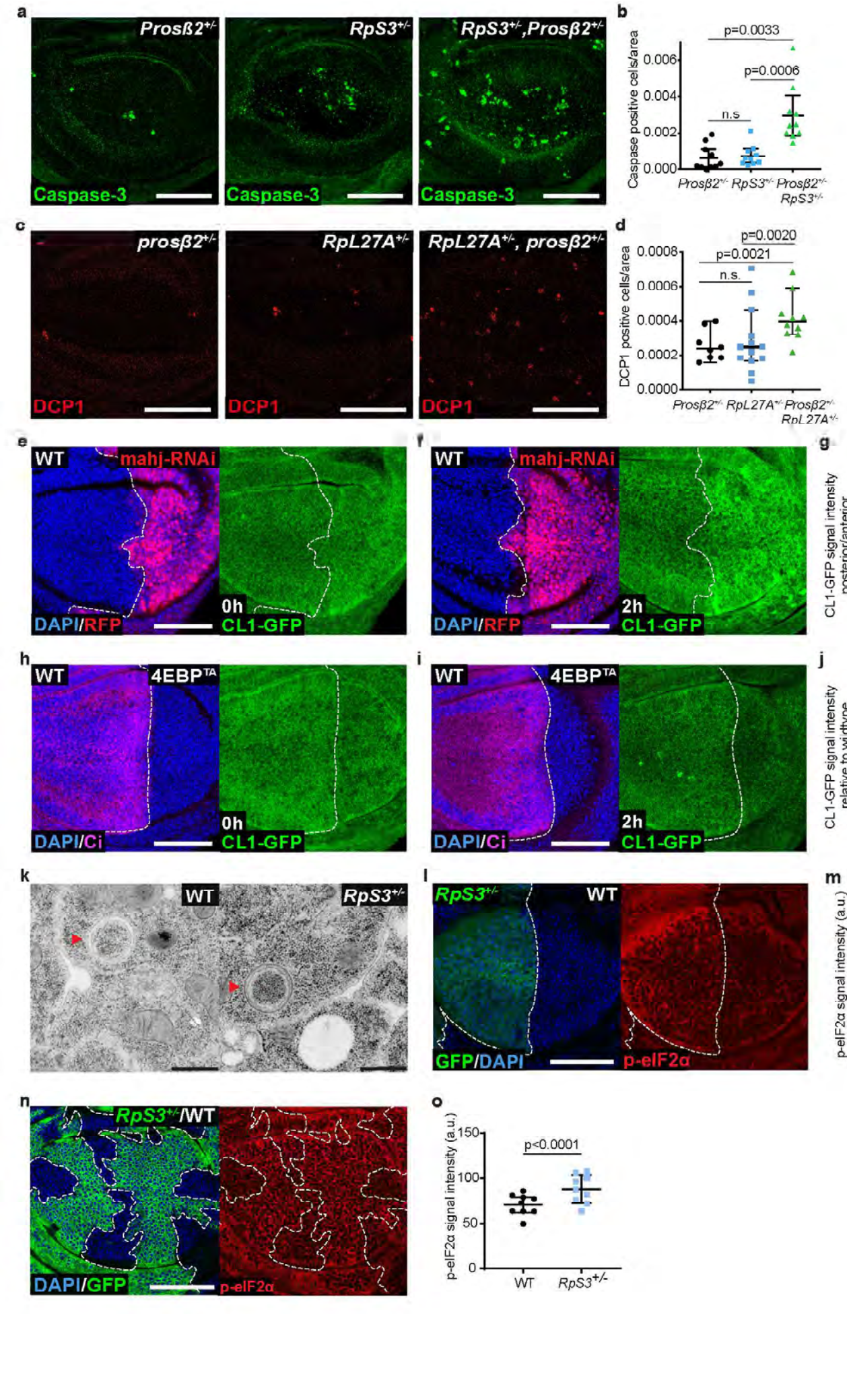
a
Prosß2+/-
RpS3+/-
RpS3+/-,Prosβ2+/-
Caspase-3
Caspase-3
Caspase-3
b
p=0.0033
p=0.0006
n.s
Caspase positive cells/area
0.006
0.004
0.002
0.000
Prosβ2+/-
RpS3+/-
Prosβ2+/- RpS3+/-
c
prosβ2+/-
RpL27A+/-
RpL27A+/-, prosβ2+/-
DCP1
DCP1
DCP1
d
p=0.0020
p=0.0021
n.s.
DCP1 positive cells/area
0.0008
0.0006
0.0004
0.0002
0.0000
Prosβ2+/-
RpL27A+/-
Prosβ2+/- RpL27A+/-
e
WT
mahj-RNAi
DAPI/RFP
0h
CL1-GFP
f
WT
mahj-RNAi
DAPI/RFP
2h
CL1-GFP
g
p=0.0012
CL1-GFP signal intensity posterior/anterior
1.6
1.4
1.2
1.0
0h
2h
Time after heatshock
h
WT
4EBPTA
DAPI/Ci
0h
CL1-GFP
i
WT
4EBPTA
DAPI/Ci
2h
CL1-GFP
j
p=0.0006
p=0.0001
p=0.0258
CL1-GFP signal intensity relative to widtype
2.5
2.0
1.5
1.0
0.5
0h
2h
0h
2h
RpS3+/-
UAS-4EBPTA
k
WT
RpS3+/-
l
RpS3+/-
WT
GFP/DAPI
p-eIF2α
m
p=0.0313
p-eIF2α signal intensity (a.u.)
100
50
0
WT
RpS3+/-
n
RpS3+/-/WT
DAPI/GFP
p-eIF2α
o
p<0.0001
p-eIF2α signal intensity (a.u.)
150
100
50
0
WT
RpS3+/-

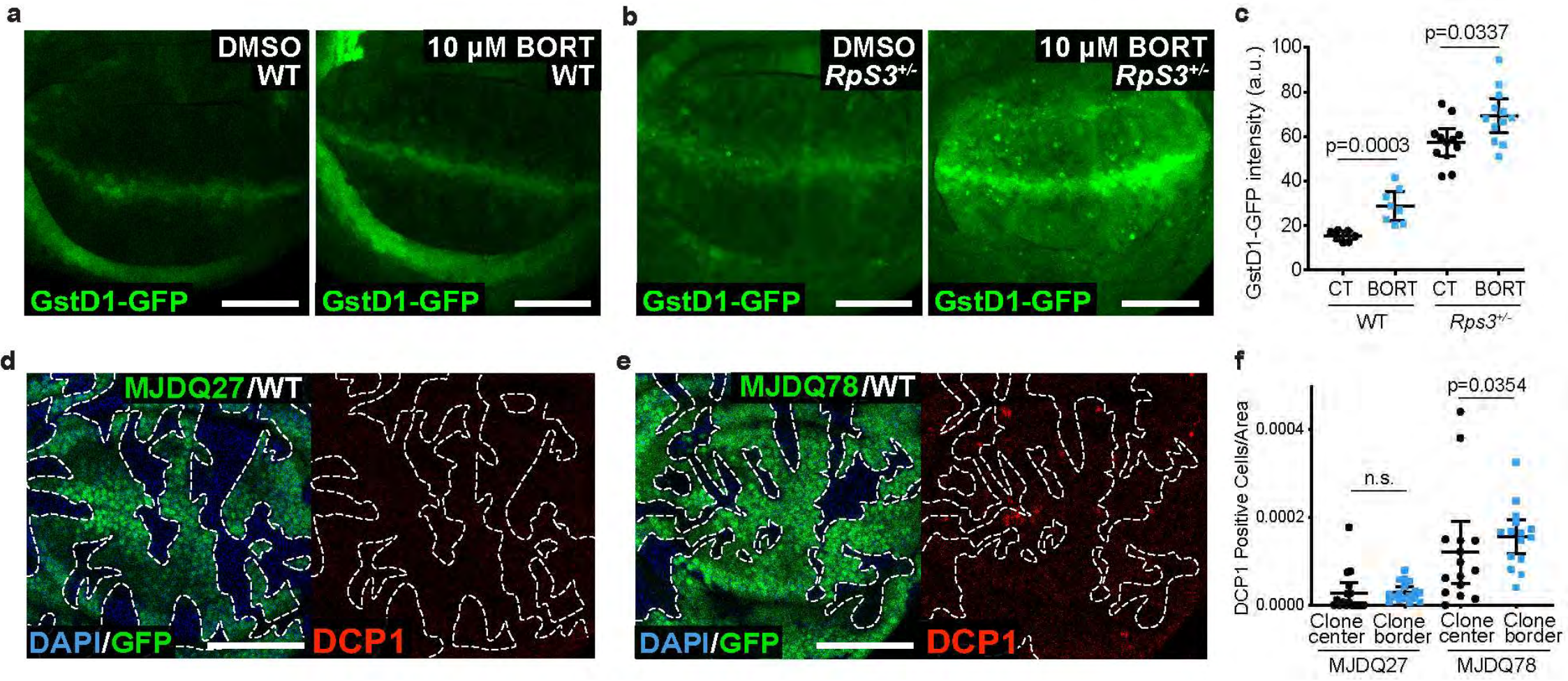
a
DMSO
WT
GstD1-GFP
10 µM BORT
WT
GstD1-GFP
b
DMSO
RpS3+/-
GstD1-GFP
10 µM BORT
RpS3+/-
GstD1-GFP
c
GstD1-GFP intensity (a.u.)
100
80
60
40
20
0
p=0.0003
p=0.0337
CT
BORT
CT
BORT
WT
Rps3+/-
d
MJDQ27/WT
DAPI/GFP
DCP1
e
MJDQ78/WT
DAPI/GFP
DCP1
f
DCP1 Positive Cells/Area
0.0004
0.0002
0.0000
n.s.
p=0.0354
Clone center
Clone border
Clone center
Clone border
MJDQ27
MJDQ78

Supplementary Table 1: Genes Differentially Expressed in JNK-inhibited vs JNK-Competent *R* and/or Unfolded Protein Res

Flybase ID	baseMean	baseMeanA	baseMeanB	foldChange
FBgn0037363	729.9686512	857.895553	644.68405	0.75147149
FBgn0035871	2911.093424	2586.75265	3127.32061	1.20897551
FBgn0266717	3341.157454	4734.04767	2412.56398	0.50961971
FBgn0261108	614.6677406	738.832145	531.891471	0.71990841
FBgn0041171	3087.252066	3669.84514	2698.85669	0.73541433
FBgn0001229	242.6957176	84.5314897	348.138536	4.1184479
FBgn0038651	1517.545637	1780.8894	1341.98313	0.75354658
FBgn0004177	12456.47849	13894.5896	11497.7378	0.82749747
FBgn0034691	502.8745858	580.559601	451.084576	0.77698237
FBgn0264357	1305.968171	1512.67977	1168.16044	0.77224569
FBgn0000546	1934.569955	2271.77143	1709.76897	0.75261487
FBgn0260936	2755.394797	3109.12439	2519.57507	0.81038092
FBgn0022027	700.6554139	581.62374	780.009864	1.34109014
FBgn0010638	5935.767143	4848.29158	6660.75085	1.37383463
FBgn0261014	12642.64026	14794.3629	11208.1585	0.75759657
FBgn0020618	40188.92389	32970.6391	45001.1138	1.36488449
FBgn0266411	2422.272403	3059.27533	1997.60379	0.65296633
FBgn0031049	3115.65665	2292.96574	3664.11726	1.59798168
FBgn0026317	1055.60221	1280.86342	905.428069	0.70688885
FBgn0029840	1143.327745	1440.76628	945.03539	0.65592553
FBgn0039969	1595.360121	1317.53832	1780.57466	1.35144051
FBgn0039966	362.7577252	286.643353	413.50064	1.44256142
FBgn0044452	872.3920328	1081.11765	733.241619	0.67822555
FBgn0039749	57.19633646	38.3390108	69.7678869	1.81976231
FBgn0034009	878.5676128	1033.3322	775.391222	0.75037943
FBgn0262656	2491.90582	3200.84293	2019.28108	0.63085916
FBgn0086357	11239.95786	9471.06641	12419.2188	1.31127988
FBgn0262516	282.1412346	330.820728	249.688239	0.75475392
FBgn0035542	304.7599756	464.949062	197.967252	0.42578267
FBgn0027492	4889.528189	5453.11827	4513.80147	0.82774685
FBgn0000257	443.8182671	557.015364	368.353536	0.6612987
FBgn0030812	1685.891616	2138.55849	1384.1137	0.64721807
FBgn0010303	1297.782669	1575.86644	1112.39349	0.70589325
FBgn0003079	1107.539098	1340.8124	952.02356	0.71003487
FBgn0043884	6175.468358	8001.56571	4958.07013	0.61963749
FBgn0003392	2227.686666	2546.97911	2014.82504	0.79106461
FBgn0023143	13899.65	16296.4639	12301.7741	0.75487383
FBgn0038816	481.1665917	655.647881	364.845732	0.55646597
FBgn0005198	1208.354591	1454.30437	1044.38808	0.71813583
FBgn0040491	11.4673959	21.1199382	5.03236767	0.23827568
FBgn0021796	1955.828633	2334.81583	1703.17051	0.72946675
FBgn0052350	1014.219166	1174.01528	907.688424	0.77314873
FBgn0260439	9409.874135	10769.1083	8503.718	0.78963994
FBgn0265988	564.5226888	710.922878	466.922563	0.65678371
FBgn0025802	635.2609425	767.870222	546.854756	0.71217081

FBgn0032200	2663.448018	2277.65183	2920.64548	1.2823055
FBgn0000346	267.6667287	339.258002	219.939213	0.64829484
FBgn0035871	2911.093424	2586.75265	3127.32061	1.20897551
FBgn0001230	1544.760194	327.799689	2356.0672	7.18752115
FBgn0032480	987.0020988	1187.17181	853.555626	0.71898239
FBgn0051414	33.97843758	50.1062788	23.2265434	0.46354557
FBgn0051354	2053.897594	386.437015	3165.53798	8.19160137
FBgn0030873	1372.52166	1164.31162	1511.32836	1.29804455
FBgn0023511	966.9396468	1154.78757	841.707698	0.72888531
FBgn0013279	2000.731479	374.043904	3085.18986	8.24820248
FBgn0013278	2349.220237	394.518599	3652.35466	9.25775026
FBgn0013277	1804.670991	429.024649	2721.76855	6.34408434
FBgn0013276	3593.796257	921.628993	5375.2411	5.83232639
FBgn0013275	3460.852546	899.12626	5168.67007	5.74854756
FBgn0261984	932.6959586	1105.67106	817.379225	0.73926076
FBgn0047135	4792.886195	4050.44202	5287.84898	1.30549924
FBgn0028692	6176.020089	6941.31724	5665.82199	0.81624594
FBgn0028694	4538.980647	3996.40724	4900.69625	1.22627549
FBgn0032884	2741.779234	2124.16791	3153.52012	1.48459079
FBgn0250843	5528.735543	4849.85045	5981.3256	1.23330104
FBgn0036136	1271.155611	1449.28439	1152.40309	0.79515318
FBgn0086134	5568.679942	4780.63934	6094.04034	1.27473334
FBgn0033698	1598.10726	2005.84529	1326.28191	0.66120848
FBgn0023174	4969.922245	4291.74185	5422.04251	1.26336641
FBgn0028688	3401.475306	2980.25384	3682.28962	1.23556241
FBgn0028687	4008.243903	3308.35749	4474.83485	1.35258504
FBgn0016756	2814.273551	3911.47479	2082.80606	0.53248613
FBgn0031652	172.9232895	138.684144	195.749387	1.41147633
FBgn0261456	1813.781009	2090.78597	1629.11103	0.77918594
FBgn0031528	16.33450531	3.4431678	24.9287303	7.24005677
FBgn0259685	4027.850445	4748.12283	3547.66886	0.74717293
FBgn0030674	4286.686499	5970.40066	3164.21039	0.52998292
FBgn0036913	637.0777616	776.216957	544.318298	0.70124505
FBgn0266717	3341.157454	4734.04767	2412.56398	0.50961971
FBgn0028692	6176.020089	6941.31724	5665.82199	0.81624594
FBgn0028694	4538.980647	3996.40724	4900.69625	1.22627549
FBgn0028500	1082.883681	1232.45536	983.169229	0.79773212
FBgn0041171	3087.252066	3669.84514	2698.85669	0.73541433
FBgn0028467	505.7955589	602.373286	441.410408	0.7327855
FBgn0038660	1160.591245	1347.06643	1036.27446	0.76928237
FBgn0032884	2741.779234	2124.16791	3153.52012	1.48459079
FBgn0250848	6974.25661	5917.34448	7678.8647	1.29768762
FBgn0029996	1730.019475	2093.94929	1487.3996	0.7103322
FBgn0039214	2289.76443	2965.70159	1839.13966	0.62013645
FBgn0032480	987.0020988	1187.17181	853.555626	0.71898239
FBgn0032467	2075.514867	2361.39727	1884.9266	0.79822511
FBgn0250843	5528.735543	4849.85045	5981.3256	1.23330104
FBgn0017418	1028.689886	1252.30568	879.612692	0.70239456
FBgn0052850	822.0384789	620.988087	956.072074	1.53959809
FBgn0260962	4139.169281	4761.34196	3724.3875	0.78221382
FBgn0260940	531.5854584	452.795234	584.112275	1.29001419
FBgn0260936	2755.394797	3109.12439	2519.57507	0.81038092

FBgn0037842	575.5070859	483.78051	636.658136	1.31600617
FBgn0022027	700.6554139	581.62374	780.009864	1.34109014
FBgn0026597	2358.912377	2641.94034	2170.22707	0.82145196
FBgn0261014	12642.64026	14794.3629	11208.1585	0.75759657
FBgn0031107	1205.842386	1652.37955	908.150941	0.5496019
FBgn0000273	1822.114502	2057.40227	1665.25599	0.80939737
FBgn0031057	4034.45473	4711.82626	3582.87371	0.76040022
FBgn0024222	515.1267583	600.296744	458.346768	0.76353366
FBgn0029763	1621.906113	1884.32848	1446.95787	0.76789046
FBgn0029856	297.8690754	460.516126	189.437708	0.41135955
FBgn0086558	9639.740828	7078.04656	11347.537	1.6032018
FBgn0030320	1842.066755	2105.27179	1666.59673	0.7916302
FBgn0004391	1379.723421	1553.76644	1263.69474	0.81331062
FBgn0036136	1271.155611	1449.28439	1152.40309	0.79515318
FBgn0039749	57.19633646	38.3390108	69.7678869	1.81976231
FBgn0034071	1426.761309	1715.40778	1234.33033	0.71955505
FBgn0259174	1717.01028	2114.58566	1451.96003	0.68664044
FBgn0259152	1297.471767	1684.62622	1039.3688	0.61697295
FBgn0262517	1730.374145	1982.83312	1562.06816	0.78779608
FBgn0086134	5568.679942	4780.63934	6094.04034	1.27473334
FBgn0029093	4705.185504	3961.70571	5200.8387	1.31277765
FBgn0032208	4105.170465	4693.98134	3712.62988	0.79093409
FBgn0028476	1105.880312	1312.68972	968.007372	0.73742283
FBgn0030057	963.6034972	665.298037	1162.4738	1.74729781
FBgn0040291	148.3632378	106.160863	176.498155	1.66255389
FBgn0015024	6003.6949	7186.871	5214.91083	0.72561631
FBgn0050421	605.1824832	705.074813	538.587597	0.76387298
FBgn0003557	1152.955202	1307.08594	1050.20138	0.80346773
FBgn0260794	4560.851195	6389.26865	3341.90623	0.52304988
FBgn0037659	2480.722788	2938.46196	2175.56334	0.74037485
FBgn0030873	1372.52166	1164.31162	1511.32836	1.29804455
FBgn0030809	2826.576425	3478.47814	2391.97528	0.68764994
FBgn0005632	3734.308077	4956.79414	2919.31737	0.58895272
FBgn0261786	782.6120388	909.633609	697.930992	0.76726606
FBgn0033916	550.2156991	652.976065	481.708789	0.73771278
FBgn0023511	966.9396468	1154.78757	841.707698	0.72888531
FBgn0033738	890.031137	1016.77777	805.533381	0.79224134
FBgn0023174	4969.922245	4291.74185	5422.04251	1.26336641
FBgn0011706	274.6842702	368.283145	212.28502	0.57641796
FBgn0028688	3401.475306	2980.25384	3682.28962	1.23556241
FBgn0028687	4008.243903	3308.35749	4474.83485	1.35258504
FBgn0261931	684.5089227	884.467295	551.203341	0.62320376
FBgn0033260	2069.158216	2388.32647	1856.37938	0.77727204
FBgn0025720	1532.715771	1283.41383	1698.91707	1.32374845
FBgn0035959	611.2413624	742.891455	523.474634	0.70464485
FBgn0030366	3276.640922	4031.90482	2773.13165	0.6877969
FBgn0011230	5903.143503	6897.08343	5240.51689	0.75981637
FBgn0003942	35392.17608	29701.3805	39186.0398	1.31933396
FBgn0003941	33670.76822	28941.8432	36823.3849	1.27232342
FBgn0021796	1955.828633	2334.81583	1703.17051	0.72946675
FBgn0027053	2092.358829	1817.66131	2275.49051	1.25187817
FBgn0032640	3282.86616	2896.57778	3540.39175	1.22226711

FBgn0020257	4191.510026	4822.1305	3771.09638	0.78203947
FBgn0015589	985.108809	1254.94839	805.215754	0.64163257
FBgn0027512	1127.371706	1284.17078	1022.83899	0.79649764
FBgn0027508	1229.600297	1471.18068	1068.54671	0.72631915

'*pS3*$^{+/-}$ Cells With Associated With Protein Catabolism, Proteasome, Autophagy, ponse GO Terms

log2FoldChange	pval	padj	symbol	GO
-0.412209721	0.003964	0.027398915	Atg17	GOBP:autophagy
0.273785023	0.00838	0.048419233	BI-1	GOBP:autophagy
-0.972507034	1.93E-14	3.25E-12	Bruce	GOBP:autophagy
-0.474114733	0.000147	0.002057175	Atg13	GOBP:autophagy
-0.443370815	0.008303	0.048057042	ago	GOBP:autophagy
2.042100739	1.18E-28	6.21E-26	Hsp67Bc	GOBP:autophagy
-0.408231396	0.00016	0.002208433	CG14299	GOBP:autophagy
-0.273173192	0.00459	0.030501137	mts	GOBP:autophagy
-0.364046226	0.00547	0.034787939	Synj	GOBP:autophagy
-0.372868182	0.002554	0.019662639	SNF4Agamı	GOBP:autophagy
-0.410016292	0.000883	0.008676736	EcR	GOBP:autophagy
-0.303327892	0.00305	0.022496927	scny	GOBP:autophagy
0.423406212	0.000717	0.007394443	Vps25	GOBP:autophagy
0.458208351	5.06E-06	0.000125619	Sec61beta	GOBP:autophagy
-0.400498301	3.15E-05	0.000589822	TER94	GOBP:autophagy
0.448778858	3.82E-05	0.000682303	Rack1	GOBP:autophagy
-0.614919488	0.000188	0.002513911	sima	GOBP:autophagy
0.676250872	8.68E-06	0.000200474	Sec61gamn	GOBP:autophagy
-0.500444712	1.01E-05	0.000227807	Tsc1	GOBP:autophagy
-0.608396057	5.23E-08	2.60E-06	raptor	GOBP:autophagy
0.434498005	7.94E-05	0.001245118	Fis1	GOBP:autophagy
0.528632741	0.000329	0.004012845	Rab21	GOBP:autophagy
-0.560162952	1.62E-06	4.82E-05	Atg2	GOBP:autophagy
0.863750027	0.004731	0.031262995	CG11498	GOBP:autophagy
-0.414307824	0.000391	0.004577633	CG8155	GOBP:autophagy
-0.664610139	9.83E-05	0.001483762	dm	GOBP:autophagy
0.390975647	0.002947	0.021935815	Sec61alpha	GOBP:autophagy
-0.40592176	0.008509	0.048982772	Trpml	GOBP:autophagy
-1.231810872	5.09E-13	7.10E-11	DOR	GOBP:autophagy
-0.272738479	0.005937	0.0370168	wdb	GOBP:autophagy
-0.59662603	9.52E-06	0.000215946	car	GOBP:autophagy
-0.627676211	9.92E-08	4.51E-06	CG8949	GOBP:autophagy
-0.502478068	5.01E-06	0.000124903	hep	GOBP:autophagy
-0.494038218	1.12E-05	0.000249157	phl	GOBP:autophagy
-0.690503651	6.35E-08	3.11E-06	mask	GOBP:autophagy
-0.338132559	0.00117	0.010802171	shi	GOBP:autophagy
-0.405692562	2.39E-05	0.000468987	Uba1	GOBP:autophagy
-0.845634638	9.39E-06	0.000214176	Lrrk	GOBP:autophagy
-0.477671347	1.75E-05	0.000360907	gig	GOBP:autophagy
-2.069296379	0.001318	0.011812175	Buffy	GOBP:autophagy
-0.45508588	1.50E-05	0.000318585	Tor	GOBP:autophagy
-0.371182122	0.001147	0.010677893	CG32350	GOBP:autophagy
-0.340733141	0.000436	0.004960801	Pp2A-29B	GOBP:autophagy
-0.606509757	2.18E-05	0.000434278	mv	GOBP:autophagy
-0.489704796	8.20E-05	0.0012798	Sbf	GOBP:autophagy

0.358740016	0.001689	0.014278517	CG5676	GOBP:autophagy
-0.625277998	6.10E-05	0.001003835	comt	GOBP:autophagy
0.273785023	0.00838	0.048419233	BI-1	GOBP:response_to_unfolded_protein
2.845494297	2.75E-112	3.33E-108	Hsp68	GOBP:response_to_unfolded_protein
-0.475971657	0.000108	0.001593513	Edem2	GOBP:response_to_unfolded_protein
-1.10921693	0.007779	0.04577929	CG31414	GOBP:response_to_unfolded_protein
3.034145511	2.47E-52	2.73E-49	Hsp70Bbb	GOBP:response_to_unfolded_protein
0.376339903	0.000735	0.007509983	CG15814	GOBP:response_to_unfolded_protein
-0.456236267	7.13E-05	0.001140905	Edem1	GOBP:response_to_unfolded_protein
3.04407975	2.16E-39	1.54E-36	Hsp70Bc	GOBP:response_to_unfolded_protein
3.210661644	1.26E-40	1.02E-37	Hsp70Bb	GOBP:response_to_unfolded_protein
2.66541195	3.99E-50	3.73E-47	Hsp70Ba	GOBP:response_to_unfolded_protein
2.544071459	3.91E-10	3.32E-08	Hsp70Ab	GOBP:response_to_unfolded_protein
2.523197488	1.03E-10	9.80E-09	Hsp70Aa	GOBP:response_to_unfolded_protein
-0.435844761	0.002396	0.018735455	Ire1	GOBP:response_to_unfolded_protein
0.384601618	0.00332	0.024004011	CG32276	GOBP:response_to_unfolded_protein
-0.292924192	0.002865	0.021522664	Rpn2	GOCC:proteasome_complex
0.294283128	0.003656	0.025819057	Rpn11	GOCC:proteasome_complex
0.570065321	0.000333	0.004052621	Pomp	GOCC:proteasome_complex
0.302524993	0.003708	0.026048442	Prosalpha6	GOCC:proteasome_complex
-0.330695285	0.002715	0.020584763	Ufd1-like	GOCC:proteasome_complex
0.35019548	0.001575	0.013490523	Prosalpha2	GOCC:proteasome_complex
-0.596822876	2.48E-08	1.35E-06	CG8858	GOCC:proteasome_complex
0.337273124	0.001058	0.010020919	Prosbeta2	GOCC:proteasome_complex
0.305167883	0.002966	0.0220384	Rpn7	GOCC:proteasome_complex
0.435719304	1.99E-05	0.000402553	Rpt1	GOCC:proteasome_complex
-0.909184157	3.54E-19	1.13E-16	Ubp64E	GOBP:protein_catabolic_process
0.497204939	0.008086	0.047172659	jet	GOBP:protein_catabolic_process
-0.359960453	0.000671	0.007003891	hpo	GOBP:protein_catabolic_process
2.85600101	1.93E-05	0.000392329	CG15412	GOBP:protein_catabolic_process
-0.420485904	0.00567	0.035726545	crb	GOBP:protein_catabolic_process
-0.915982222	8.92E-17	1.90E-14	CG8184	GOBP:protein_catabolic_process
-0.512009417	0.00011	0.001625111	CG8334	GOBP:protein_catabolic_process
-0.972507034	1.93E-14	3.25E-12	Bruce	GOBP:protein_catabolic_process
-0.292924192	0.002865	0.021522664	Rpn2	GOBP:protein_catabolic_process
0.294283128	0.003656	0.025819057	Rpn11	GOBP:protein_catabolic_process
-0.326023723	0.003913	0.027124108	Rich	GOBP:protein_catabolic_process
-0.443370815	0.008303	0.048057042	ago	GOBP:protein_catabolic_process
-0.448537143	0.00062	0.006616451	CG11070	GOBP:protein_catabolic_process
-0.37841485	0.000723	0.007426578	CG14291	GOBP:protein_catabolic_process
0.570065321	0.000333	0.004052621	Pomp	GOBP:protein_catabolic_process
0.375943142	0.000159	0.002192274	26-29-p	GOBP:protein_catabolic_process
-0.493434215	3.44E-06	9.07E-05	UbcE2H	GOBP:protein_catabolic_process
-0.6893424	2.61E-11	2.73E-09	puf	GOBP:protein_catabolic_process
-0.475971657	0.000108	0.001593513	Edem2	GOBP:protein_catabolic_process
-0.325132428	0.00383	0.026753656	CG9934	GOBP:protein_catabolic_process
0.302524993	0.003708	0.026048442	Prosalpha6	GOBP:protein_catabolic_process
-0.509646429	7.60E-06	0.000178	ari-1	GOBP:protein_catabolic_process
0.622553789	3.33E-07	1.28E-05	CG32850	GOBP:protein_catabolic_process
-0.354365064	0.000387	0.004540581	pic	GOBP:protein_catabolic_process
0.367386932	0.005592	0.035393781	lsn	GOBP:protein_catabolic_process
-0.303327892	0.00305	0.022496927	scny	GOBP:protein_catabolic_process

0.396166253	0.002407	0.018778946	CG6567	GOBP:protein_catabolic_process
0.423406212	0.000717	0.007394443	Vps25	GOBP:protein_catabolic_process
-0.28375189	0.006264	0.03866191	Axn	GOBP:protein_catabolic_process
-0.400498301	3.15E-05	0.000589822	TER94	GOBP:protein_catabolic_process
-0.863541106	6.49E-15	1.21E-12	HERC2	GOBP:protein_catabolic_process
-0.305079928	0.004051	0.027851465	Pka-C1	GOBP:protein_catabolic_process
-0.395169149	7.50E-05	0.001190318	Ubqn	GOBP:protein_catabolic_process
-0.389236345	0.002845	0.021419809	ird5	GOBP:protein_catabolic_process
-0.381027569	0.000384	0.004521274	CG4165	GOBP:protein_catabolic_process
-1.281528146	2.03E-11	2.20E-09	CG11700	GOBP:protein_catabolic_process
0.680956037	1.29E-08	7.61E-07	Ubi-p5E	GOBP:protein_catabolic_process
-0.337101445	0.00147	0.012823147	CG2247	GOBP:protein_catabolic_process
-0.298121644	0.006585	0.040051633	shtd	GOBP:protein_catabolic_process
-0.330695285	0.002715	0.020584763	Ufd1-like	GOBP:protein_catabolic_process
0.863750027	0.004731	0.031262995	CG11498	GOBP:protein_catabolic_process
-0.47482303	2.72E-05	0.00052288	CG8405	GOBP:protein_catabolic_process
-0.542373269	3.49E-07	1.33E-05	Nedd4	GOBP:protein_catabolic_process
-0.696720862	2.25E-10	2.04E-08	Clbn	GOBP:protein_catabolic_process
-0.344105857	0.001266	0.011488039	l(3)76BDr	GOBP:protein_catabolic_process
0.35019548	0.001575	0.013490523	Prosalpha2	GOBP:protein_catabolic_process
0.392622579	0.000105	0.001565251	cathD	GOBP:protein_catabolic_process
-0.33837061	0.001889	0.015603996	CG5604	GOBP:protein_catabolic_process
-0.43943601	0.000936	0.009080583	CG15817	GOBP:protein_catabolic_process
0.805125523	1.59E-11	1.77E-09	Ppt1	GOBP:protein_catabolic_process
0.733401102	0.003533	0.025186264	Roc1b	GOBP:protein_catabolic_process
-0.462721205	2.32E-05	0.00045621	CkIalpha	GOBP:protein_catabolic_process
-0.388595337	0.004186	0.028370974	CG30421	GOBP:protein_catabolic_process
-0.315688011	0.004911	0.032051704	Su(dx)	GOBP:protein_catabolic_process
-0.934979551	3.44E-08	1.79E-06	ctrip	GOBP:protein_catabolic_process
-0.433672206	2.57E-05	0.000500275	Kdm2	GOBP:protein_catabolic_process
0.376339903	0.000735	0.007509983	CG15814	GOBP:protein_catabolic_process
-0.540253771	0.000656	0.006883543	CG9086	GOBP:protein_catabolic_process
-0.763776283	7.21E-14	1.14E-11	faf	GOBP:protein_catabolic_process
-0.382201162	0.001387	0.012266678	mi	GOBP:protein_catabolic_process
-0.438868864	0.000638	0.00677159	CG8494	GOBP:protein_catabolic_process
-0.456236267	7.13E-05	0.001140905	Edem1	GOBP:protein_catabolic_process
-0.335988117	0.004056	0.027851465	DUBAI	GOBP:protein_catabolic_process
0.337273124	0.001058	0.010020919	Prosbeta2	GOBP:protein_catabolic_process
-0.7948128	2.63E-07	1.06E-05	rpr	GOBP:protein_catabolic_process
0.305167883	0.002966	0.0220384	Rpn7	GOBP:protein_catabolic_process
0.435719304	1.99E-05	0.000402553	Rpt1	GOBP:protein_catabolic_process
-0.682224165	2.33E-08	1.27E-06	CG42797	GOBP:protein_catabolic_process
-0.363508479	0.000511	0.005640119	Cul4	GOBP:protein_catabolic_process
0.404628996	0.00024	0.003077717	Ate1	GOBP:protein_catabolic_process
-0.5050318	5.55E-05	0.000925226	CG4911	GOBP:protein_catabolic_process
-0.539945473	8.63E-08	4.03E-06	Usp7	GOBP:protein_catabolic_process
-0.396277303	5.42E-05	0.000911322	poe	GOBP:protein_catabolic_process
0.399809793	0.001669	0.014145039	RpS27A	GOBP:protein_catabolic_process
0.347465445	0.004075	0.027872041	RpL40	GOBP:protein_catabolic_process
-0.45508588	1.50E-05	0.000318585	Tor	GOBP:protein_catabolic_process
0.324094167	0.002378	0.018624095	CSN5	GOBP:protein_catabolic_process
0.2895596	0.004894	0.032027097	Sgt	GOBP:protein_catabolic_process

-0.354686674	0.000382	0.004503224	ppa	GOBP:protein_catabolic_process
-0.64018073	1.46E-07	6.28E-06	Apc	GOBP:protein_catabolic_process
-0.328258016	0.003584	0.025441752	CG10254	GOBP:protein_catabolic_process
-0.461324471	0.00022	0.002883496	Tnks	GOBP:protein_catabolic_process

Supplementary Table 2: Key Experimental Resources

Antibodies		
Rabbit anti-pJNK pTPpY (used 1:500)	Promega	Cat#V793B
Rat anti-Ci (used 1:1000)	DSHB	Cat#2A1
Rabbit anti-Ref(2)P (used 1:2000)	Tor Erik Rusten [63]	N/A
Rabbit anti-cleaved Caspase-3 (used 1:25000)	Abcam	Cat#13847
Rabbit anti-Dcp1 (used 1:2500)	Cell signalling	Cat#9578S
Rabbit anti-p-eif2 α (used 1:500)	Cell signaling	Cat#3398T
Mouse anti-FK2 (used 1:5000)	Merck	Cat#04-263
Drosophila Strains		
Drosophila RpS3[Plac92]	Bloomington	Cat#BL5627
*Drosophila RpS3**	Bloomington	Cat#BL5699
Drosophila RpL27A[1]	Bloomington	Cat#BL5697
Drosophila hs-FLP;; FRT82B	Daniel St. Johnston	N/A
y [1],w[1118]	Daniel St. Johnston	N/A
en-Gal4, UAS-FLP; FRT82B	[24]	N/A
hh-Gal4/TM6b	Jean-Paul Vincent	N/A
Drosophila FRT42D, ubi-GFP/Cyo	Bloomington	Cat#BL5697
FRT82B, RpS3[Plac92], hh-Gal4	[24]	N/A
Drosophila hs-FLP, UAS-CD8-GFP;; FRT82B, RpS3[Plac92], act>RpS3>Gal4/TM6b	This paper	N/A
Drosophila tub-Gal80 ^{TS}	Bloomington	Cat#BL7016
Drosophila UAS-GFP-atg8-mCherry	Bloomington	Cat#BL37749
Drosophila FRT42D mahj	[31]	N/A
Drosophila UAS-puc	E. Martinez Blanco	N/A
Drosophila UAS-4E-BP^{TA}	[29]	N/A
Drosophila w+/w-; tub>CD2>Gal4, UAS-GFP; tub-Gal80 ^{TS}	Bruce Edgar	N/A
Drosophila hs-FLP ^{122};; act>CD2>Gal4, UAS-GFP/TM6b	Bruce Edgar	N/A
Drosophila UAS-GADD34	FlyORF	Cat#F003018
Drosophila UAS-dFOXO	Bloomington	Cat#BL9575

Drosophila Pros β2 EP3067 /TM6b	Bloomington	Cat#BL6787
Drosophila UASp-GFP-mCherry-Atg8a	Bloomington	Cat#BL37749
Drosophila hsflp;; FRT82B atg13/TM6b	Tor Erik Rusten	N/A
Drosophila UAS-Atg1 RNAi	Harvard TRiP	HMS02750
Drosophila UAS-Atg9-RNAi	Bloomington	Cat#BL28055
Drosophila UAS-p62-RNAi	Bloomington	Cat#BL33978
Drosophila UAS-Rpt6 RNAi	VDRC	Cat#49244/GD
Drosophila Atg8a KG07569 /FM7c	Bloomington	Cat#BL14639
Drosophila Ref(2)P od2 /CyO	64	N/A
Drosophila UAS-mahj RNAi	Bloomington	Cat#BL34912
Drosophila GstD1-GFP	33	N/A
Drosophila hs-CL1-GFP (ProteoFLUX)	This paper	N/A
Drosophila hs-p62-GFP(ReFLUX)	This paper	N/A
Drosophila UAS-Hsap/MJD-Q27	Bloomington	Cat#BL8149
Drosophila UAS-Hsap/MJD-Q78	Bloomington	Cat#BL8150
Oligonucleotides		
Primer: CAAGAAGAGAACTCTGAATAGGG	This paper	pUAST_p62_F1
Primer: CAAGTAAATCAACTGCAACTACT	This paper	pUAST_p62_F2
Primer: GAGTATAAATAGAGGCGTTCG	This paper	pUAST_p62_F3
Primer: CCATTCATCAGTTCCATAGGTTG	This paper	pUAST_p62_R1
Primer: GTCACACCACAGAAGTAAGGTTC	This paper	pUAST_p62_R2
Primer: CAGAGAAGGAGGCAAACAG	This paper	pUAST_p62_R3
Primer: TGAATAGGGAATTGGGAATTCAATAGGGAATTGGGAATTCTAGCGC	This paper	CL1-GFP_InfusF
Primer: GCTGGAATTAGGCCTTCTAGACGGCGGCAGATCCTCAC	This paper	CL1-GFP_InfusR

Primer: TCGATCCCCGGGTACCCGGC GATCTTGAAGTTCCTATTCCC AAGTTCCTATTCCGAAGTTC TATTCTCTAGAAAGTATAGGA ACTTCAGAGCGCTTCAAAATG AATGCGAACCTTCCGATTTC	This paper	RpS3_FusL
CTGCCTTTTTACAAAACTTTC CCTCGGACAGA	This paper	RpS3_FusR
TTTGTAAAAAGGCAGATCGAA TTCGAGCT	This paper	αT_H70_FusL
TCCCGGATCTGGTACCAGCT CAAAAGCGCTCTGAAGT	This paper	αT_H70_FusR

Supplementary Table 3: Experimental Genotypes and Conditions

Figure/Panel	Genotype	Heat shock duration, time between heat shock and dissection (water bath temperature)
Main figures		
1a (left)	*yw*	N/A
1a (right)	*FRT82B, RpS3[Plac92], ubi-GFP/+*	N/A
1c	*hs-FLP;; FRT82B, RpS3[Plac92], ubi-GFP/FRT82B*	10 min, 72 hours
1e	*hs-FLP;; FRT82B, RpS3[Plac92], ubi-GFP/FRT82B*	10 min, 72 hours
1f	*hs-FLP; tub>CD2>Gal4, UAS-CD8-GFP/+; tub-Gal80^{TS}/UAS-4E-BP^{TA}*	40 min, 72 hours (29 °C)
1h	*hs-FLP; tub>CD2>Gal4, UAS-CD8-GFP/+; tub-Gal80^{TS}/UAS-4E-BP^{TA}*	40 min, 72 hours (29 °C)
1j	*en-Gal4, UAS-FLP/+; FRT82B, RpS3[Plac92], ubi-GFP/FRT82B*	N/A
1k	*hh-Gal4/UAS-4E-BP^{TA}*	N/A
1l	*en-Gal4, UAS-FLP/GstD1-GFP; FRT82B, RpS3[Plac92], tub-dsRed/FRT82B*	N/A
1m	*GstD1-GFP/+; hh-Gal4/UAS-4E-BP^{TA}*	N/A
1o	*GstD1-GFP/+; FRT82B, RpS3[Plac92], hh-Gal4/UAS-GADD34*	N/A
1q	*hs-FLP, UAS-CD8-GFP/+;; FRT82B, RpS3[Plac92], act>RpS3>Gal4/+*	25 min, 72 hours
1r	*hs-FLP, UAS-CD8-GFP/+;; FRT82B, RpS3[Plac92], act>RpS3>Gal4/UAS-GADD34*	25 min, 72 hours
2a (left)	*p62^{od2}/+*	N/A
2a (middle)	*FRT82B, RpS3[Plac92], tub-dsRed/+*	N/A
2a (right)	*p62^{od2}/+; FRT82B, RpS3[Plac92], tub-dsRed/+*	N/A
2c (left)	*UAS-GFP-mCherry-atg8a/GstD1-GFP; hh-Gal4/+*	N/A
2c (right)	*UAS-GFP-mCherry-atg8a/+; hh-Gal4/ FRT82B, RpS3[Plac92], ubi-GFP*	N/A
2d	*en-Gal4, UAS-FLP/+; FRT82B, RpS3[Plac92], tub-dsRed/FRT82B*	N/A
2f	*hs-FLP; FRT42D mahj/FRT42D, ubi-GFP*	1 hour, 72 hours
2g	*hh-Gal4/UAS-4E-BP^{TA}*	N/A
2i-j	*hs-GFP-p62/+; en-Gal4, UAS-FLP/+; FRT82B, RpS3[Plac92], tub-dsRed/FRT82*	N/A
2l-m	*hs-GFP-p62/+; en-Gal4, UAS-RFP/+; tub-Gal80^{TS}/UAS-mahj RNAi*	(27°C)
3a	*hs-FLP; UAS-atg1 RNAi/+; act>CD2>Gal4, UAS-GFP/+*	40 min, 72 hours
3c	*hs-FLP; UAS-atg1 RNAi/+; act>CD2>Gal4, UAS-GFP/+*	40 min, 72 hours
3d	*GstD1-GFP/UAS-atg1 RNAi; hh-Gal4/+*	N/A
3e-f	*hs-FLP;; FRT82B atg13/FRT82B ubi-GFP*	25 min, 72 hours
3j	*hs-FLP; tub>CD2>Gal4, UAS-CD8-GFP/+; UAS-Atg9-RNAi/+*	40 min, 72 hours
3k	*hs-FLP; tub>CD2>Gal4, UAS-CD8-GFP/+; UAS-Atg9-RNAi/UAS-4E-BP^{TA}*	40 min, 72 hours
4a	*yw*	N/A

4b	*FRT82B, RpS3[Plac92], ubi-GFP/+*	N/A
4e	*hs-CL1-GFP/+; en-Gal4, UAS-RFP/UAS-Rpt6 RNAi; Gal80^{TS}/+*	(29°C)
4g-h	*hs-CL1-GFP/+; en-Gal4, UAS-FLP/+; FRT82B, RpS3[Plac92], tub-dsRed/FRT82*	N/A
4k	*en-Gal4, UAS-FLP/+; FRT82B, RpS3*/FRT82B*	N/A
4l	*en-Gal4, UAS-FLP/+; FRT82B, RpS3[Plac92], ubi-GFP/FRT82B*	N/A
5a-b	*hs-FLP/+;; FRT82B, RpS3[Plac92], ubi-GFP/FRT82B*	12 min, 54 hours
5d-e	*GstD1-GFP/+; FRT82B, RpS3[Plac92], tub dsRed/+*	N/A
5f	*tub-Gal80^{TS}/+; UAS-dFOXO/+; FRT82B, RpS3[Plac92], hh-Gal4/+*	(27.5C)
5g	*hs-FLP; tub>CD2>Gal4, UAS-CD8-GFP/UAS-dFOXO; FRT82, RpS3[Plac92], tub-dsRed/+*	N/A
5i	*UAS-dFOXO/+; FRT82B, RpS3[Plac92], tu dsRed/hh-Gal4, tub-Gal80^{ts}*	(26.5°C)
5k	*hs-FLP, UAS-CD8-GFP/+;; FRT82B, RpS3[Plac92], act>RpS3>Gal4/+*	40 min, 72 hours
5l	*hs-FLP, UAS-CD8-GFP/+; UAS-dFOXO/+; FRT82B, RpS3[Plac92], act>RpS3>Gal4/+*	40 min, 72 hours
6a	*GstD1-GFP/UAS-MJDQ78; hh-Gal4/+*	N/A
6c	*hs-p62-GFP; UAS-MJDQ78/+; hh-Gal4/+*	N/A
6d	*GstD1-GFP/UAS-MJDQ78; hh-Gal4/+*	N/A
6f	*hs-FLP; UAS-MJDQ78/+; act>CD2>Gal4, UAS-GFP/+*	30 min, 72 hours
6h	*hs-FLP/+; tub>CD2>Gal4, UAS-CD8-GFP/UAS-MJDQ78*	40 min, 72 hours
6k	*hs-FLP;; act>CD2>Gal4, UAS-GFP/+*	12 min, 96 hours
6l	*hs-FLP; UAS-MJDQ78/+; act>CD2>Gal4, UAS-GFP/+*	12 min, 96 hours
Extended data figures		
ED1a	*hs-FLP;; FRT82B, RpS3[Plac92], ubi-GFP/FRT82B*	12 min, 48 hours
ED1b	*hs-FLP; tub>CD2>Gal4, UAS-CD8-GFP/+; tub-Gal80^{TS}/UAS-4E-BP^{TA}*	40 min, 72 hours (29 °C)
ED1d	*en-Gal4, UAS-RFP/+; tub-Gal80^{TS}/UAS-mahj RNAi*	(27°C)
ED1f	*GstD1-GFP/+; FRT82B, RpS3[Plac92], hh-Gal4/UAS-GADD34*	N/A
ED1h	*GstD1-GFP/+; FRT82B, RpS3[Plac92], hh-Gal4/UAS-GADD34*	N/A
ED2a	*GstD1-GFP/+; FRT82B, RpS3[Plac92], Hh-Gal4/UAS-puc*	N/A
ED2b (left)	*Atg8a^{KG07569} /+*	N/A
ED2b (middle)	*FRT82B, RpS3[Plac92], ubi-GFP/+*	N/A
ED2b (right)	*Atg8a^{KG07569} /+;; FRT82B, RpS3[Plac92], ubi GFP/+*	N/A
ED2d (left)	*FRT82B, atg13/+*	N/A
ED2d (middle)	*FRT82B, RpS3[Plac92], ubi-GFP/+*	N/A
ED2d (right)	*FRT82B, RpS3[Plac92], ubi-GFP/FRT82B atg13*	N/A
ED2f (left)	*p62^{od2} /+*	N/A
ED2f (middle)	*GFP, RpL27A[1], FRT40A/+*	N/A
ED2f (right)	*p62^{od2} / GFP, RpL27A[1], FRT40A*	N/A

ED2h (left)	*hs-FLP, UAS-CD8-GFP/+;; FRT82B, RpS3[Plac92], act>RpS3>Gal4/+*	25 min, 72 hours
ED2h (middle)	*hs-FLP, UAS-CD8-GFP/+; UAS-Atg1 RNAi/+; FRT82B, RpS3[Plac92], act>RpS3>Gal4/+*	25 min, 72 hours
ED2h (right)	*hs-FLP, UAS-CD8-GFP/+;; FRT82B, RpS3[Plac92], act>RpS3>Gal4/UAS-Atg9 RNAi*	25 min, 72 hours
ED3a-b	*hs-GFP-p62/+; UAS-atg1 RNAi/+; hh-Gal4/+*	N/A
ED3d	*hs-FLP/hs-GFP-p62;; FRT82B, RpS3[Plac92], tub-dsRed/FRT82B*	15 min, 72 hours
ED3g-h	*hs-GFP-p62/+; en-Gal4, UAS-FLP/+; FRT82B, RpS3[Plac92], tub-dsRed/FRT82*	N/A
ED3i-j	*hs-GFP-p62/+;; hh-Gal4/UAS-4E-BP^{TA}*	N/A
ED4a (left)	*Prosβ2^{EP3067}/+*	N/A
ED4a (middle)	*FRT82B, RpS3[Plac92], tub>dsRed/+*	N/A
ED4a (right)	*FRT82B, RpS3[Plac92], tub>dsRed/ Prosβ2^{EP3067}*	N/A
ED4c (left)	*Prosβ2^{EP3067}/+*	N/A
ED4c (middle)	*GFP, RpL27A[1], FRT40A /+*	N/A
ED4c (right)	*GFP, RpL27A[1], FRT40A /+; Prosβ2^{EP3067}/+*	N/A
ED4e-f	*hs-CL1-GFP; enGal4, UAS-RFP/+; tub-Gal80^{TS}/UAS-mahj RNAi*	(27^{o}C)
ED4h-i	*hs-CL1-GFP;; hh-Gal4/UAS-4E-BP^{TA}*	N/A
ED4k	*en-Gal4, UAS-FLP/+; FRT82B, RpS3[Plac92], ubi-GFP/FRT82B*	N/A
ED4l	*en-Gal4, UAS-FLP/+; FRT82B, RpS3[Plac92], ubi-GFP/FRT82B*	N/A
ED4n	*hs-FLP, UAS-CD8-GFP/+;; FRT82B, RpS3[Plac92], act>RpS3>Gal4/+*	25min, 72 hours
ED5a	*yw, GstD1-GFP /+*	N/A
ED5b	*GstD1-GFP/+; FRT82B, RpS3[Plac92], tub dsRed/+*	N/A
ED5d	*hs-FLP; UAS-MJDQ27/+; act>CD2>Gal4, UAS-GFP/+*	30min, 72 hours
ED5e	*hs-FLP; UAS-MJDQ78/+; act>CD2>Gal4, UAS-GFP/+*	30min, 72 hours